Article:
Cheng, J, Dong, Z, Zhu, H et al. (6 more authors) (2022) Synthesis and ceramisation of organometallic precursors for Ta4HfC5 and TaHfC2 ultra-fine powders through a facile one-pot reaction. Journal of Alloys and Compounds, 989. 162989. ISSN 0925-8388

https://doi.org/10.1016/j.jallcom.2021.162989

Synthesis and ceramisation of organometallic precursors for Ta_4HfC_5 and $TaHfC_2$ ultra-fine powders through a facile one-pot reaction

Jun Cheng[a], Zhijun Dong[a*], Hui Zhu[a], Guanming Yuan[a], Aidan Westwood[b], Ye Cong[a], Baoliu Li[a], Jianguang Guo[a], Xuanke Li[a*]

[a] The Hubei Province Key Laboratory of Coal Conversion & New Carbon Materials, Wuhan University of Science and Technology, Wuhan, Hubei 430081, PR China

[b] School of Chemical and Process Engineering, University of Leeds, Leeds, LS2 9JT, U.K.

Abstract

Ultra-fine Ta_4HfC_5 and $TaHfC_2$ powders were prepared through the pyrolysis of a precursor synthesised by using a facile one-pot reaction. $HfCl_4$, $TaCl_5$, and phenolic resins were used as the sources of hafnium (Hf), tantalum (Ta), and carbon (C), respectively. The as-synthesised precursors were further utilised to prepare Ta_4HfC_5- and $TaHfC_2$-modified carbon/carbon (C/C-Ta_4HfC_5 and C/C-$TaHfC_2$) composites through precursor infiltration and pyrolysis. The transformation of Ta_4HfC_5 and $TaHfC_2$ precursors into ultra-fine ceramic powders and anti-ablation performance of the C/C-Ta_4HfC_5 and C/C-$TaHfC_2$ composites were investigated. The carbothermal reduction of Ta_2O_5 and $Hf_6Ta_2O_{17}$ and the solid solution reaction between HfC and TaC occur

∗ Corresponding author. Tel/ Fax: +86 27 68862676.
E-mail address: dongzj72@sohu.com (Z.J. Dong)
∗ Corresponding author. Tel/ Fax: +86 27 68862676.
E-mail address: xkli@21cn.com (X.K. Li)

successively during the pyrolysis of Ta_4HfC_5 precursors. HfC and TaC undergo a sufficient solid solution reaction at 1800 °C to form the Ta_4HfC_5 solid solution with a particle size of 200–300 nm. The pyrolysis products of $TaHfC_2$ precursors acquired at 1400–1600 °C are composed of TaC, HfC and $TaHfC_2$. High-temperature pyrolysis promotes the solid solution reaction between TaC and HfC. The $TaHfC_2$ solid solution with a particle size of 100–150 nm is formed at 1800 °C. The introduction of $TaHfC_2$ and Ta_4HfC_5 solid solutions into the C/C composite substantially enhances their anti-ablation performance. The linear ablation rates of C/C-Ta_4HfC_5 and C/C-$TaHfC_2$ are 11.04 and 16.97 μm/s, respectively, which are considerably lower than that of the C/C composite. The good anti-ablation performance of the C/C-Ta_4HfC_5 and C/C-$TaHfC_2$ composites can be attributed to the formation of the Ta_2O_5 and $Hf_6Ta_2O_{17}$.

Keywords： Ta_4HfC_5; $TaHfC_2$; Carbothermal reduction; Pyrolysis; Anti-ablation

I. Introduction

TaC and HfC, with the NaCl-type structure, are categorised into ultra-high temperature ceramics (UHTCs) having excellent properties such as high hardness, high melting point, high elastic modulus, good electrical conductivity, and chemical attack resistance. UHTCs present a potential in extreme applications. For example, they can be used as diffusion barriers in nuclear industry and the leading edges of hypersonic vehicles [1-3]. Through the reaction between TaC and HfC, a continuous single-phase solid solution Ta–Hf–C with face-centred-cubic structure can be formed. This solid

solution has various compositions, and Ta_4HfC_5 derived from 4TaC–HfC has the highest melting point (4215 K) among refractory materials. This is probably because Hf(Ta) 5d- and C 2p-like states are strongly hybridised [4]. Moreover, the hardness of $(Ta_{0.8}Hf_{0.2})C_{1+x}$ at high temperatures positively deviates from the calculated value according to the rule of mixtures and exceeds that of both TaC_{1-x} and HfC_{1+x} [5]. Because of its high melting point and hardness, Ta_4HfC_5 is a promising material for aerospace applications. It can be utilised to fabricate composite rocket boosters or surface coatings applied in ultra-high-temperature environments.

To date, various preparation methods, such as spark plasma sintering (SPS) [6], hot pressing sintering [5], and pressure-less sintering [7], for Ta_4HfC_5 solid solution are proposed. However, high temperatures and long production periods are required for these methods, and the prepared Ta_4HfC_5 powders usually have a large grain size, which results in relatively poor sinterability and is detrimental to some mechanical properties such as thermal shock resistance and flexural strength [8]. By contrast, the sol–gel method allows an efficient low-temperature synthesis of ultra-fine ceramic powders resulting from intimate contact between reactants. Simonenko et al. [9, 10] reported a hybrid method for Ta_4HfC_5 nanocrystal fabrication. In their method, the first step is to hydrolyse precursors in a controlled manner by using a polymeric carbon source to produce a gel. Subsequently, the gel is dried and subjected to preliminary heat treatment to obtain a starting mixture of metal oxide and carbon, which is chemically reactive and highly dispersed. Finally, carbothermal reduction is performed at low temperature. However, several drawbacks, such as relatively long aging time, poor sol stability, and

process complexity, remain in the sol–gel method. As a result, its wide application is restricted [11].

The preceramic polymer technique is an alternative approach to fabricate ultra-fine ceramic powders. It is widely adopted for the manufacturing of carbon fibre-reinforced ceramic matrix composites, which is accomplished through polymer impregnation and pyrolysis (PIP). The solution-derived precursor has the characteristic of homogeneous distribution of its various components at the atomic or molecular level, which causes the pyrolytic conversion of the polymeric precursor to occur at low temperatures and to be completed in a short duration [12, 13]. Jiang et al. [2] reported the fabrication of ultra-fine Ta_4HfC_5 powders through solvothermal processing combined with carbothermal reduction by using an inorganic hybrid. However, this synthesis route has the disadvantages of a complex process and low ceramic yield. Moreover, controlling the particle size and morphology of Ta_4HfC_5 powders is considerably difficult. Lu et al. [1] reported the preparation of nanoscale Ta_4HfC_5 ceramics by curing and pyrolysing the precursor polymers synthesised through the cohydrolysis and polycondensation of tantalum and hafnium alkoxides coordinated with acetyl acetone, followed by the mixing of the acquired intermediate product with a phenolic resin (carbon source). However, this method involves a cumbersome multi-step curing reaction and long synthesis period, which limits its further industrial application. Therefore, creative strategies with the characteristics of simple, rapid, and efficient synthesis are worth pursuing from the perspective of large-scale industrial applications.

This paper reports a facile one-pot method for the synthesis of Ta_4HfC_5 and $TaHfC_2$ organometallic precursors by using commercially available $TaCl_5$, $HfCl_4$, and phenolic resins as raw materials. Compared with the aforementioned traditional preceramic polymer approaches, the one-pot method proposed in this study presents the advantages of simple process, high ceramic yield (~60 wt%), and short synthesis period (2–3 h). All chemical reactions are completed in one reactor, avoiding the separation and transfer of intermediate products. Additionally, Hf and Ta atoms form a short-range structure at the molecular level through polycondensation instead of through simple physical mixing. This is conducive to improving precursor stability and achieving the highly uniform distribution of Ta and Hf atoms during precursor pyrolysis, which ultimately accelerates the formation of Ta_4HfC_5 and $TaHfC_2$ solid solutions. Taking into consideration the readily available raw materials, simple process route with a high ceramic yield and convenient operation, the proposed one-pot method can be used for the large-scale industrial production of Ta_4HfC_5 and $TaHfC_2$ precursors.

$TaHfC_2$ precursors are also prepared in this study considering the fact that $TaHfC_2$ has the highest elastic modulus and hardness among TaC-HfC solid solutions, but its preparation by employing organometallic precursors is seldom reported [14]. The resulting Ta_4HfC_5 and $TaHfC_2$ precursors are further used to prepare Ta_4HfC_5- and $TaHfC_2$-modified carbon/carbon (C/C-Ta_4HfC_5 and C/C-$TaHfC_2$) composites through PIP to enhance the ablation resistance of C/C composites. The conversion of Ta_4HfC_5 and $TaHfC_2$ organometallic precursors into ultra-fine ceramics and their microstructural evolution are investigated. On the basis of the results, the solid solution mechanism of

Ta_4HfC_5 and $TaHfC_2$ ceramics is proposed. Finally, the ablation resistances of C/C-Ta_4HfC_5 and C/C-$TaHfC_2$ composites are tested and analysed..

2. Experimental procedures

2.1 Raw materials

All the chemical reagents used were of analytical grade and were employed as received. Tantalum pentachloride ($TaCl_5$, purity 99%, Zhengzhou JACS Chemical Product Co., Ltd, Zhengzhou, China), hafnium chloride ($HfCl_4$, purity 99.9%, Zhengzhou JACS Chemical Product Co., Ltd, Zhengzhou, China), ethanol (analytical reagent, Chengdu Kelong Chemical Reagent Factory, Chengdu, China), and acetylacetone (Hacac, analytical reagent, Chengdu Kelong Chemical Reagent Factory, Chengdu, China) were used to synthesise Ta_4HfC_5 and $TaHfC_2$ precursors. We used the THC-400 phenolic resin (carbon yield: approximately 60 wt%) obtained from Taihang Impedefire Polymer Co. Ltd, Shanxi, China, as the carbon source.

2.2 Synthesis of organometallic precursors for Ta_4HfC_5 and $TaHfC_2$

The synthesis of Ta_4HfC_5 and $TaHfC_2$ ultra-fine powders from their organometallic precursors is illustrated in Fig. 1. Approximately 36 g of $TaCl_5$ (0.1 mol) and 8 g of $HfCl_4$ (0.025 mol) were dissolved in a mixture comprising ethanol (100 mL) and 0.25 mol acetylacetone (25 mL) for the electrostatic ion-interaction-assisted production of the precursor containing tantalum and hafnium. Subsequently, 4 g phenolic resin was dissolved in ethanol (20 mL), and then the resulting mixture added into the precursor containing tantalum and hafnium with magnetic stirring. Afterwards,

the resulting solution was refluxed at 200 °C for 2 h in an oil bath in a flowing argon atmosphere. During this process, the liquid Ta_4HfC_5 precursor formed through the coordination between the hydroxyl group in the phenolic resin and tantalum- and hafnium-containing species, and the solution colour changed from light yellow to reddish brown. Finally, the remaining water and ethanol were removed from the liquid Ta_4HfC_5 precursor through vacuum distillation. The $TaHfC_2$ organometallic precursor was synthesised in a similar manner with the following modifications: the molar ratio of $TaCl_5$ (9 g) to $HfCl_4$ (8 g) used was 1:1, and the amount of phenolic resin added was approximately 2 g.

2.3 Pyrolysis of Ta_4HfC_5 and $TaHfC_2$ precursors

Ta_4HfC_5 and $TaHfC_2$ precursors were subjected to solidification at 200 °C through the removal of residual ethanol and water. Subsequently, pyrolysis was performed in a vertical induction furnace for 1 h at required temperatures (400–1800 °C) at a heating rate of 10 °C/min under flowing argon conditions. We deemed the yield of ceramics to be the ratio of the pyrolysed product mass to original cured precursor mass at 200 °C.

2.4 Fabrication of the C/C-Ta_4HfC_5 and C/C-$TaHfC_2$ composites

First, porous C/C substrates (Φ30 mm × 10 mm) with a density of approximately 1.2 g/cm^3 were obtained by impregnating a carbon fibre felt with coal tar pitch, followed by carbonisation. The impregnation and carbonisation temperatures were 250 and 1000 °C, respectively. The synthesised liquid Ta_4HfC_5 and $TaHfC_2$ precursors were impregnated into porous C/C substrates. Afterwards, these specimens were subjected to pyrolysis to convert the precursors into Ta_4HfC_5 and $TaHfC_2$ ceramics. Pyrolysis was

performed in a graphite resistance furnace in a flowing argon atmosphere at 1800 °C for 1 h. After 10–12 cycles of PIP, the C/C-Ta_4HfC_5 and C/C-$TaHfC_2$ composites with a density of approximately 2.0 g/cm^3 were obtained and used for ablation tests.

2.5 Ablation test

The ablation test of the C/C-Ta_4HfC_5 and C/C-$TaHfC_2$ composites was conducted on a plasma generator (Multiplaz 3500) with an operation voltage of 160 (±1) V and a current of 6 A. The inner diameter of the plasma nozzle was 2 mm, and the distance between the centre of the specimen surface and nozzle tip was approximately 10 mm. The temperature at the centre of the sample was measured with an optical pyrometer, and its maximum value was approximately 3000 °C. The ablation time was set to 75 s. The mass and linear ablation rates were calculated according to changes in the mass and thickness of the specimens before and after the test [15].

2.6 Characterisation

To monitor structural variations during pyrolysis, a Fourier-transform infrared spectrometer (FTIR, VERTEX70, Bruker) was utilised for recording the spectra of precursors and their pyrolysed products within a range of 4000–400 cm^{-1}. A Nuclear Magnetic Resonance spectrometer (NMR, DD2 600M, Agilent) was used to collect the ^{1}H NMR and ^{13}C NMR data of the precursor by using deuterated dimethyl sulfoxide (DMSO-d6) as a solvent. X-ray photoelectron spectroscopy (XPS, MultiLab 2000, VG) was employed for analysing the chemical states of pyrolysis products, and the instrument was provided with a monochromatic X-ray source (Al Kα, 300 W). XPSPEAK41 software was used for XPS fitting, and XPS binding energies were

calibrated with respect to the C 1s photoelectric peak at 284.6 eV. XPS fitting mainly includes revising the peak position of C 1s, adding the baseline, adding peaks, fitting the peaks, etc. The details for XPS fitting are available in reference [16]. An X-ray diffraction (XRD) system (X'Pert ProMPD, Philips), which employed Cu-Kα radiation (λ = 1.54056 Å) emitted using a Cu target working at 40 kV and 40 mA, was utilised for the phase composition identification of the pyrolysis products and ablated C/C-Ta_4HfC_5 and C/C-$TaHfC_2$ composites. Rietveld refinement was conducted by employing the General Structure Analysis System (GSAS) program to acquire the lattice parameters of the Ta–Hf–C solid solution [17]. For precursor pyrolysis tracing, differential scanning calorimetry (DSC) combined with thermogravimetry analysis (TGA-DSC, STA 449C, Netzsch) was performed at the heating rate of 10 °C/ min in the argon atmosphere. The morphologies of the pyrolysis products and C/C-Ta_4HfC_5 and C/C-$TaHfC_2$ composites were observed with field emission scanning electron microscopy (FESEM, NOVA400 NANOSEM), which was combined with energy dispersive spectroscopy (EDS). The microstructure of the pyrolysis products was further elucidated through high-resolution transmission electron microscopy (HRTEM, JEM-2010 UHR JEOL, Japan), and the instrument was provided with an EDS attachment (EDSINCA IE 350 Penta FET X-3, Oxford, UK) working at 300 kV. In HRTEM analyses, initially, the samples were pulverised, and then, were dispersed through ultrasonic vibrations by using an ethanol solution. Afterwards, the dispersion (one drop) was placed on a copper grid, followed by air drying for subsequent analyses.

3. Results and discussion

3.1 FTIR and NMR characterisations of the Ta_4HfC_5 precursor and its pyrolysis products

To understand chemical structure transformation, FTIR analysis was performed on the as-synthesised Ta_4HfC_5 precursor and its products pyrolysed at various temperatures (Fig. 2). For the Ta_4HfC_5 precursor, the wide absorption spectrum appearing at 2700–3600 cm^{-1} is assigned to the –OH stretching vibration from the moisture absorbed in the sample (Fig. 2a). The intense peaks observed at approximately 1625, 1505, and 1364 cm^{-1} correspond to the stretching vibration of C=O, the stretching vibration of C=C, and the bending vibration of $–CH_3$ in the acetylacetone ligand, respectively, suggesting that Hf- and Ta-chelate structures are present in the precursor. The peaks obtained at 1437 and 756 cm^{-1} are assigned to the stretching vibrations of C=C and C–H in the benzene rings of the phenolic resin, respectively. However, the band observed at 865 cm^{-1} can be ascribed to the Hf–O and Ta–O stretching vibrations resulting from the precursor with Ta–O–Ta and Hf–O–Hf bridges. The spectrum appearing at approximately 610 cm^{-1} is attributed to both the Ta–O (Ta–O–C chain) and Hf–O (Hf–O–C chain) stretching vibrations, and the peaks observed at 454 and 510 cm^{-1} are linked to the asymmetric stretching vibration of Hf–O [18]. In addition, a weak band appears at 1105 cm^{-1}, which can be tentatively assigned to C–O stretching vibration in both the Ta–O–C and Hf–O–C chains. The emergence of these peaks signifies the smooth incorporation of tantalum and hafnium into the formed polymer backbone. The FTIR spectrum of the precursor after the heat treatment at 200 °C (Fig. 2b) shows a

resemblance to that of the Ta_4HfC_5 precursor. However, the widening and attenuation of peaks suggest that the precursor is dehydrated and carbonised. With an increase in pyrolysis temperature to 400 °C, the peaks centred at 3256 and 865 cm^{-1} disappear (Fig. 2c), indicating that the precursor is further dehydrated and carbonised. With a further increase in pyrolysis temperature from 400 to 600 °C, the peaks associated with the phenolic resin and ligand acetylacetone almost completely disappear, except those observed at approximately 660 and 510 cm^{-1} (Fig. 2d). This phenomenon indicates nearly complete damage of the polymer backbone at 600 °C and the complete conversion of the organic precursor into inorganic constitution.

The ^{1}H NMR and ^{13}C NMR data were collected to further analyse the chemical structure of the Ta_4HfC_5 precursor. Fig. 3a shows the ^{1}H NMR spectra of the phenolic resin and Ta_4HfC_5 precursor. For the phenolic resin, ^{1}H NMR signals appear in three discrete intervals. The multiplets between 3.0 and 4.0 ppm, between 1.2 and 4.8 ppm, and between 8 and 10 ppm can be assigned to $–CH_2–$, aromatic hydrogen, and phenolic –OH groups, respectively. The spectrum of the Ta_4HfC_5 precursor is similar to that of the phenolic resin. However, additional peaks are observed in the Ta_4HfC_5 precursor. The peak observed at 1.0 ppm corresponds to $CH_3CH_2O–$ form, and the peaks located at 1.99 and 2.09 ppm can be attributed to CH_3CO-ketone from acetylacetone ligand [12]. This finding indicates that the Hf- and Ta-chelate structures exist in the precursor. Moreover, phenolic –OH multiplets from the phenolic resin are not detected in the Ta_4HfC_5 precursor, which may be due to the chelation of phenolic –OH with tantalum/hafnium ions. Fig. 3b presents the ^{13}C NMR spectra of the phenolic resin and

Ta_4HfC_5 precursor. In the spectrum of the phenolic resin, the multiple peaks ranging from 23.0 and 34.0 ppm correspond to the aliphatic $–CH_2–$ form. The multiple peaks between 100.0 and 160.0 ppm are caused by aromatic carbon. The ^{13}C NMR spectrum of the Ta_4HfC_5 precursor reveals the peaks of aliphatic $–CH_2–$ and aromatic carbon appearing in the phenolic resin. In addition, two strong peaks at 18.5 and 50.1 ppm and two weak peaks at 31.0 and 203.5 ppm, which are assigned to $CH_3CH_2O–$ and CH_3CO- ketone from acetylacetone ligand, respectively, appear in the Ta_4HfC_5 precursor. This coincides with the results of ^1H NMR spectra.

The possible synthesis route for the Ta_4HfC_5 and $TaHfC_2$ precursors was predicted according to the aforementioned FTIR and NMR findings and previous reports. This route may include chelation and polycondensation. Metal–cation chelation involves heteroatom complex formation through the reaction between tantalum/hafnium ions, hydroxyl groups, and Hacac functional groups, according to Eqs. (1) and (2) (Fig. 4) [18, 19]. Because many reactive hydroxyl groups are available in the molecular chain of the phenolic resin, it has a strong ability to form complexes with metals [20]. During the mixing of tantalum- and hafnium-containing precursors with the phenolic resin at 200 °C, the coordination of tantalum/hafnium ions with two or more hydroxyl groups occurs in the chains of the phenolic resin through an ion-exchange mechanism according to Eq. (3) (Fig. 4) [19]. Additionally, self-polycondensation reactions can occur according to Eqs. (4) and (5) (Fig. 4), which leads to the formation of polymers with Ta–O–Ta and Hf–O–Hf bridges [19, 21]. This finding is consistent with the FT-IR results. The polycondensation reactions induce a uniform distribution of tantalum,

hafnium, carbon, and oxygen in the synthetic precursor at the atomic scale. This distribution level cannot be attained only by blending and reacting tantalum and hafnium sources with a carbon source.

3.2 XRD and XPS analyses of the Ta_4HfC_5 precursor and its pyrolysis products

The phase evolution of the product was traced by adopting XRD during the pyrolysis of the Ta_4HfC_5 precursor. Fig. 5a shows the XRD spectra for the Ta_4HfC_5 precursor after 600–1800 °C pyrolysis. At 600 °C, no perceivable diffraction peaks appear for the pyrolysis product, suggesting that the product has an amorphous structure. At 800 °C, the amorphous product transforms into crystalline oxides. The diffraction peaks assigned to Ta_2O_5 (JCPDS card No. 89-2843) appear. In addition, feeble diffraction peaks attributed to solid solution $Hf_6Ta_2O_{17}$ (JCPDS card No. 44-0998) are detected. No discernible diffraction peaks from HfO_2 are observed. Newly formed stable-phase $Hf_6Ta_2O_{17}$ can result from the solid solution reaction between HfO_2 and Ta_2O_5. As the pyrolysis temperature increases to 1000 °C, the intensity of Ta_2O_5 and $Hf_6Ta_2O_{17}$ diffraction peaks increases, indicating that oxide crystal growth and the solid solution reaction can be promoted by increasing pyrolysis temperature. Furthermore, the weak diffraction peaks assigned to TaC (JCPDS card No. 35-0801) appear, suggesting the commencement of carbothermal reduction between pyrolytic carbon and Ta_2O_5. With the increase in pyrolysis temperature to 1200 °C, the TaC diffraction peak intensifies, and the Ta_2O_5 diffraction peak attenuates. This phenomenon can be attributed to the further consumption of Ta_2O_5 in carbothermal reduction with the free carbon, which leads to the formation of TaC. With the continuous increase in pyrolysis

temperature to 1400 °C, TaC diffraction peaks obviously shift to lower 2θ angles, indicating the formation of a solid solution of tantalum hafnium carbide ($Ta_xHf_{1-x}C$). Moreover, the diffraction peaks of Ta_2O_5 and $Hf_6Ta_2O_{17}$ disappear, and the weak diffraction peaks of HfC (JCPDS card No. 39-1491) appear. These changes may result from the probable transformation from $Hf_6Ta_2O_{17}$ into individual carbides (TaC and HfC) and the tantalum hafnium carbide solid solution ($Ta_xHf_{1-x}C$) [13]. HfC has higher initial formation temperature than TaC, indicating that TaC formation takes precedence over HfC formation in thermodynamics. With a further increase in pyrolysis temperature to 1600 and 1800 °C, the diffraction peaks of HfC disappear and those of $Ta_xHf_{1-x}C$ gradually shift to lower 2θ angles (Fig. 5b). For the XRD spectra of the pyrolysis product obtained at 1800 °C, the positions and relative intensities of all the diffraction peaks match well with the theoretical calculated values for Ta_4HfC_5 [5], which confirms the formation of the Ta_4HfC_5 solid solution. To further understand the effect of pyrolysis temperature on the crystal structure, Rietveld refinement was performed on the XRD patterns of $Ta_xHf_{1-x}C$ solid solutions. As shown in Fig. 6, the refined patterns present good agreement with the original patterns, which reveals that the refinement is reliable. Table 1 presents the refinement results. It can be seen that the lattice constant, lattice volume, and solid solubility of Hf in $Ta_xHf_{1-x}C$ solid solutions gradually increase with the increase in pyrolysis temperature. When pyrolysis temperature rises to 1800 °C, the lattice constant and solid solubility of Hf in the $Ta_xHf_{1-x}C$ solid solution become 4.484165 Å and 0.20, respectively, which agree well with the theoretical values (4.48996 Å and 0.2) calculated by Vegard's rule [2]. This

finding indicates that the solid solution reaction between HfC and TaC to form Ta_4HfC_5 completes at 1800 °C. Feng et al. [8] reported the preparation of Ta_4HfC_5 by employing a modified SPS technique with C, Ta_2O_5, and HfO_2 as starting materials. They found that the completion temperature of the solid solution reaction was 2200 °C, which is considerably higher than that observed in this study. This result can be attributed to the homogeneous distribution and intimate contact of the reactants in this study. Because the diffusion coefficient of Ta (0.31×10^{-12} m^2/s) is lower than that of Hf (0.35×10^{-12} m^2/s) [22], the diffusion rate of hafnium atoms into the TaC lattice is larger than that of tantalum atoms into the HfC lattice. Consequently, the $Ta_xHf_{1-x}C$ solid solution is highly likely to be formed through the dissolution of Hf atoms into the TaC lattice, which explains the disappearance of the HfC phase in the pyrolysis product with temperature increasing from 1400 to 1600 °C. Furthermore, the lattice parameter of $Ta_xHf_{1-x}C$ mainly depends on the radius of the dissolved hafnium atoms and the atomic ratio of tantalum to carbon (x). Because the atomic radius of Hf (2.16 Å) is larger than that of Ta (2.09 Å), the solid solution of Hf atoms into the TaC lattice leads to an increase in the lattice constant of the $Ta_xHf_{1-x}C$ solid solution. The increase in pyrolysis temperature accelerates the solid solution reaction.

To further understand the possible transformation mechanism from $Hf_6Ta_2O_{17}$ to $Ta_xHf_{1-x}C$ during Ta_4HfC_5 precursor pyrolysis, XPS analyses were conducted on the pyrolysis product obtained at 1300 °C. According to the survey spectrum shown in Fig. 7a, the pyrolysis product comprises tantalum, hafnium, carbon, and oxygen. In the curve-fitted spectrum of Ta 4f (Fig. 7b), the peaks located at 23.08 and 24.9 eV are

attributed to Ta–C bonds, and those appearing at 26.21 and 27.91 eV are ascribed to Ta–O bonds [23]. In the Hf 4f curve-fitted spectrum (Fig. 7c), the peaks located at 14.25 and 15.96 eV are assigned to Hf–C bonds, and those observed at 16.98, and 18.65 eV are caused by Hf–O bonds [24].

According to XPS combined with XRD analyses, TaC_xO_y and HfC_mO_n may be formed in the pyrolysis product at 1300 °C, and oxygen atoms are progressively substituted with carbon in the oxycarbide crystal lattice as temperature increases. The following carbothermal reduction reactions (Eqs. (6)–(10)) and solid solution reaction (Eq. (11)) may occur with the increase in pyrolysis temperature from 1200 to 1400 °C.

$$Ta_2O_5 + C \rightarrow TaC_xO_y + CO \qquad (0 < x, y < 1) \qquad (6)$$

$$TaC_xO_y + C \rightarrow TaC + CO \qquad (0 < x, y < 1) \qquad (7)$$

$$Hf_6Ta_2O_{17} + C \rightarrow TaC_xO_y + HfC_mO_n + CO \qquad (0 < x, y < 1;\ 0 < m, n < 1) \qquad (8)$$

$$TaC_xO_y + C \rightarrow TaC + CO \qquad (0 < x, y < 1) \qquad (9)$$

$$HfC_mO_n + C \rightarrow HfC + CO \qquad (0 < m, n < 1) \qquad (10)$$

$$HfC + TaC \rightarrow Ta_xHf_{1-x}C \qquad (0 < x, y < 1) \qquad (11)$$

3.3 TGA-DSC analysis of the Ta_4HfC_5 precursor

The TGA-DSC analysis was conducted to further monitor precursor-to-ceramic transformation. Fig. 8 presents the TGA-DSC curves of the Ta_4HfC_5 precursor. According to the TGA curve, the weight loss occurs in four stages. The first stage lies between the room temperature and 200 °C, the second stage ranges from 200 to 560 °C, the third stage covers the temperature range from 560 to 950 °C (although there is small weight loss in this region), and the fourth stage appears between 950 and 1200 °C. The

weight loss of approximately 15% in the first stage can be attributed to phenolic resin crosslinking as well as the evaporation of water and ethanol solvent residues. Such evaporation is also responsible for the endothermic peak (92 °C) in the DSC curve. The weight loss of approximately 18% in the second stage is assigned to the decomposition of organic groups during precursor pyrolysis. The endothermic peak near 500 °C might be caused by the organic-to-inorganic transformation of the precursor. The small weight loss in the third stage indicates that ceramisation is almost complete. The exothermic peak observed near 600 °C is due to the formation of pyrolysed carbon, amorphous Ta_2O_5, and HfO_2, and the weak exothermic peak at 800 °C may result from the conversion of amorphous Ta_2O_5 into a crystalline structure. The weak endothermic peak appeared near 930 °C can be ascribed to the formation of $Hf_6Ta_2O_{17}$ through solid solution reaction between Ta_2O_5 and HfO_2. At temperatures above 950 °C, an increasing weight loss suggests that carbothermal reduction between Ta_2O_5 and pyrolytic carbon is initiated, which is also confirmed by the XRD spectra for the pyrolysis products of the Ta_4HfC_5 precursor. At approximately 1100 °C, an evident exothermic peak appears, which may result from the formation of a large amount of TaC. At 1200 °C, the pyrolysis of the Ta_4HfC_5 precursor gives a ceramic yield of approximately 60 wt%.

3.4 Morphology of the pyrolysis products of the Ta_4HfC_5 precursor

The pyrolysis products acquired at varying temperatures of 600–1800 °C were subjected to scanning electron microscopy (SEM) and EDS analyses to understand their microstructural evolution during pyrolysis. The surface of the product pyrolysed at 600 °C is compact due to considerable volume shrinkage and amorphous state

formation (Fig. 9a). With the increase in pyrolysis temperature to 1000 °C, a large number of spherical nanocrystalline grains precipitate on the product surface due to the onset of carbothermal reduction between pyrolytic carbon and Ta_2O_5 (Fig. 9b). As the pyrolysis temperature increases from 1000 to 1200 °C, carbothermal reduction intensifies. Consequently, the spherical particles grow significantly, and the escape of CO produced by the carbothermal reaction generates many pores with various sizes (Fig. 9c). When the pyrolysis temperature rises to 1400 °C, many irregularly shaped particles with a size of approximately 100 nm are observed in addition to the small spherical particles (Fig. 9d). These particles can be identified as HfC and $Ta_xHf_{1-x}C$, according to the XRD spectra (Fig. 5). As pyrolysis temperature further rises to 1600 °C, the number of small spherical particles evidently decreases, and the irregularly shaped particles grow considerably (with a size range of 100–200 nm) due to the continuous solid solution reaction (Fig. 9e). At 1800 °C, the small spherical particles almost disappear, and the irregularly shaped particles are coarsened obviously, as indicated by particle size enlargement from 100–200 to 200–300 nm (Fig. 9f). These coarsened particles are the Ta_4HfC_5 solid solution according to the XRD result shown in Fig. 5.

The crystalline microstructure of the resulting Ta_4HfC_5 ultra-fine powders was further characterised through transmission electron microscopy (TEM) and HRTEM. Fig. 10a shows that the Ta_4HfC_5 particles tend to agglomerate and have a particle size of 200–300 nm, which agrees with the SEM observation (Fig. 9). According to the HRTEM micrograph (Fig. 10b), the Ta_4HfC_5 particles are encapsulated in an amorphous shell with a thickness of approximately 3 to 4 nm. The amorphous shell is

likely to be a carbon layer on the surface of individual carbide particles. In view of the fairly rapid diffusion of carbon atoms at high temperatures, the carbon layer is identified as residual carbon. This residual carbon is considered to suppress Ta_4HfC_5 crystal growth and coarsening by playing a role of a diffusion barrier. However, excessive residual carbon leads to the drastic deceleration of interdiffusion and considerable suppression of solid solution formation to generate individual TaC and HfC phases [14]. The highly magnified image in Fig. 10c shows a highly ordered lattice structure. The measured interplanar distance is 1.58 Å, which agrees well with the calculated value of the (220) crystal plane of Ta_4HfC_5. FFT transformation illustrated in Fig. 10d reveals the presence of spaces between (220), (420), and (422) planes in Ta_4HfC_5, which confirms the presence of the crystallised structure of the resultant solid solution at 1800 °C. This result is in agreement with the XRD findings.

To explore elemental distribution within the Ta_4HfC_5 powder, EDS mapping was performed on the pyrolysis product obtained at 1800 °C. As shown in Fig. 11, C, Ta, and Hf are homogeneously distributed over the entire sample without any obvious phase separation in the microstructure. This elemental homogeneity feature makes the one-pot reaction for polymer precursor synthesis in this study intrinsically superior to other methods. According to the aforementioned analyses of crystal structures and elemental distribution within the pyrolysis product, the pyrolysis product obtained at 1800 °C is single-phase solid solution Ta_4HfC_5 instead of a mixture of separate TaC and HfC phases. Moreover, uniform and adequate solid solution can be achieved through precursor pyrolysis at 1800 °C for 1 h.

3.5 XRD analysis of the pyrolysis products of the $TaHfC_2$ precursor

Using the same synthesis method, the $TaHfC_2$ precursor was obtained by adjusting the molar ratio of $TaCl_5$ to $HfCl_4$ to 1:1. Fig. 12a presents the XRD spectra of the pyrolysis products obtained from the $TaHfC_2$ precursor at 1400–1800 °C. For the products obtained at 1400 and 1600 °C, the peaks corresponding to individual HfC (JCPDS card No. 39-1491) and TaC (JCPDS card No. 35-0801) phases are observed. No other crystalline phases are identified. However, when the pyrolysis temperature increases to 1800 °C, the separate diffraction peaks of TaC and HfC fuse thoroughly into the peaks corresponding to a single $TaHfC_2$ solid solution phase (JCPDS card No. 89-7449). According to the fitting analysis of the peaks shown in Fig. 12b, the pyrolysis products obtained at 1400 and 1600 °C are composed of TaC, HfC, and $TaHfC_2$. The intensity of the $TaHfC_2$ peaks gradually increases with the increase in pyrolysis temperature from 1400 to 1800 °C, indicating the increase in the amount of the $TaHfC_2$ phase in the pyrolysis products. High-temperature pyrolysis accelerates the solid solution reaction between TaC and HfC, and a single-phase solid solution of $TaHfC_2$ forms at a temperature of 1800 °C.

3.6 Morphology of the pyrolysis products of the $TaHfC_2$ precursor

Fig. 13a–13d presents the morphologies for the products obtained from the $TaHfC_2$ precursor at varying pyrolysis temperatures. As shown in Fig. 13a, many nanoparticles with a size less than 30 nm are found in the product pyrolysed at 1200 °C. These particles aggregate to form irregular clusters. With the increase in pyrolysis temperature to 1400 °C, carbothermal reduction and solid solution reactions are intensified, and

consequently, the particle size increases from less than 30 to approximately 40 nm (Fig. 13b). These particles exhibit a spherical morphology and disperse homogeneously in the dark-coloured carbon substrate (amorphous). According to the XRD result (Fig. 12), these spherical particles can be identified as TaC, HfC, and $TaHfC_2$. With a further increase in pyrolysis temperature to 1600 °C, the particle size increases to approximately 60 nm (Fig. 13c). At 1800 °C, numerous particles with an irregular morphology and a size of 100–150 nm are formed because of the ongoing solid solution reaction (Fig. 13d). The EDS pattern shown in Fig. 13e indicates that the pyrolysis product acquired at 1800 °C comprises Ta, Hf, and C, with their atomic percentages of 13.42%, 14.51% and 72.07%, respectively. The atomic ratio of Ta to Hf is 13.42/14.51 (≈1/1.08), which is close to the theoretical value of the $TaHfC_2$ solid solution. However, the atomic percentage of carbon (72.07%) is higher than its corresponding theoretical value (27.93%), indicating that residual carbon exists in the pyrolysis product acquired at 1800 °C, and the ratio of bound carbon to residual carbon is approximately 0.63.

Fig. 14 presents the TEM and HRTEM images of the $TaHfC_2$ powder prepared through precursor pyrolysis at 1800 °C. The $TaHfC_2$ crystallites exhibit a uniform size distribution of 100–150 nm with some aggregation (Fig. 14a). Similar to Ta_4HfC_5, the $TaHfC_2$ particles are surrounded by an amorphous shell with a thickness of approximately 3 to 4 nm (Fig. 14b), which is considered as an amorphous carbon layer. The lattice exhibits a highly ordered feature under high magnification, and the interplanar crystal spacing (2.61 Å) coincides with the (111) space of $TaHfC_2$ (Fig. 14c). The spaces (220) and (200) in $TaHfC_2$ are also detected in FFT transformation (Fig.

14d). These results confirm the crystallised structure of the $TaHfC_2$ ultra-fine powders, which is in agreement with the XRD results.

3.7 Morphology, structure, and ablation resistance of C/C-Ta_4HfC_5 and C/C-$TaHfC_2$ composites

Fig. 15 shows the surface morphologies of the C/C-Ta_4HfC_5 and C/C-$TaHfC_2$ composites. The surfaces of the C/C-Ta_4HfC_5 and C/C-$TaHfC_2$ composites are coated with a ceramic layer (Fig. 15a and 15c). Compared with C/C-Ta_4HfC_5 composites, C/C-$TaHfC_2$ has a denser ceramic layer. Figs. 15b and 15d presents the magnified surface SEM images of the C/C-Ta_4HfC_5 and C/C-$TaHfC_2$ composites, respectively. As can be seen from the magnified SEM images, many cracks and holes, which are caused by the escape of the gas produced during precursor pyrolysis, appear on the surface of both composites. Fig. 16 presents the cross-sectional SEM images of the C/C-Ta_4HfC_5 composites. In Fig. 16a, the white area is the ceramic phase, and the grey area is the matrix carbon and carbon fibres. No obvious holes are found in the composites. The pores among fibres are filled with ceramics (Fig. 16b and 16d), and the individual fibres are coated with a ceramic layer (Fig. 16c). This finding indicates that the Ta_4HfC_5 solid solutions are introduced into the matrix of C/C composites through multiple PIP cycles.

Fig. 17 shows the photographs of C/C, C/C-Ta_4HfC_5, and C/C-$TaHfC_2$ composites before and after ablation for 75 s. Before ablation, C/C, C/C-Ta_4HfC_5, and C/C-$TaHfC_2$ composites are grey-black, brown, and black, respectively (Fig. 17a–17c). After ablation for 75 s, the colour of the C/C composites change from grey-black to grey-

white (Fig. 17d), whereas that of the C/C-Ta_4HfC_5 composites change from brown to black, and a white oxide layer covers most of their surface (Fig. 17e). For the C/C-$TaHfC_2$ composites, a continuous and complete white oxide layer is formed on its surface and flank after ablation (Fig. 17f). In addition, a large ablation pit is observed on the surface of the C/C composites, but the ablation pits are relatively smaller for the C/C-Ta_4HfC_5 and C/C-$TaHfC_2$ composites. According to the XRD results shown in Fig. 18, the white oxide layer on the surface of both the C/C-$TaHfC_2$ and C/C-Ta_4HfC_5 composites consists of $Hf_6Ta_2O_{17}$ and Ta_2O_5. The intensity of Ta_2O_5 diffraction peaks of the ablated C/C-Ta_4HfC_5 composites is considerably higher than that of the ablated C/C-$TaHfC_2$ composites. This may be because the amount of Ta_2O_5 formed by Ta_4HfC_5 oxidation is substantially larger than that formed by $TaHfC_2$ oxidation.

Table 2 presents the results of ablation test for the C/C, C/C-Ta_4HfC_5, and C/C-$TaHfC_2$ composites. Among these three composites, the C/C composites have the worst anti-ablation performance, with the linear ablation rate and mass ablation rate of 23.45 μm/s and 5.66 mg/s, respectively. The C/C-Ta_4HfC_5 composites exhibit the optimum anti-ablation performance, with the linear ablation rate and mass ablation rate of 11.04 μm/s and −1.22 mg/s, respectively. The anti-ablation performance of the C/C-$TaHfC_2$ composites is between that of C/C composites and C/C-Ta_4HfC_5 composites, with the ablation rate and mass ablation rate of 16.97 μm/s and −1.46 mg/s, respectively. The negative mass ablation rate for the C/C-Ta_4HfC_5 and C/C-$TaHfC_2$ composites indicates that the weight gain caused by Ta_4HfC_5 or $TaHfC_2$ oxidation is larger than the weight loss resulted from the oxidation of carbon fibres and matrix carbon.

Fig. 19 shows the morphologies of the ablation centres of the C/C, C/C-Ta_4HfC_5, and C/C-$TaHfC_2$ composites. For the ablated C/C composite (Fig. 19a and 19b), the carbon fibres and carbon matrix exposed to the plasma flame are severely ablated. The carbon fibres are ablated into needle-like shape, and the carbon matrix deposited on the carbon fibres is oxidised into CO_2 or CO, leading to the formation of numerous holes within the C/C composite. For the ablated C/C-Ta_4HfC_5 and C/C-$TaHfC_2$ composites (Fig. 19c and 19e), however, a molten oxide layer is formed on their surfaces. This layer acts as a barrier that inhibits the inward diffusion of oxygen. Under strong scouring action, some molten oxide is blown away by the plasma flame, and as a result a part of the carbon fibres and matrix carbon are directly exposed to the plasma flame. According to the XRD results (Fig. 18), the molten oxides constitute $Hf_6Ta_2O_{17}$ and Ta_2O_5. Fig. 19d and 19f presents the magnified SEM images of the ablation centres of the C/C-Ta_4HfC_5 and C/C-$TaHfC_2$ composites, respectively. A comparison of the morphologies of ablated C/C and C/C-Ta_4HfC_5 composites (Fig. 19a and Fig. 19d) shows that the C/C-Ta_4HfC_5 composites have less chemical oxidation damage. A small number of ablation holes are observed on the surface of the exposed carbon fibres and matrix carbon, but the carbon fibres with an oxide layer maintain their original shape (Fig. 19d). A comparison of the morphologies of ablated C/C-Ta_4HfC_5 and C/C-$TaHfC_2$ composites (Fig. 19d and Fig. 19f) reveals that the C/C-$TaHfC_2$ composites suffer more chemical oxidation damage. Most of the exposed fibres in $TaHfC_2$ composites undergo obvious oxidation, but the degree of oxidation damage is lower than that of the exposed fibres in C/C composites (Fig. 19a and 19f). The results of ablation test and SEM

observation indicate that the introduction of Ta_4HfC_5 and $TaHfC_2$ solid solutions into C/C composites considerably enhances their anti-ablation performance, and Ta_4HfC_5 presents more advantages in improving the anti-ablation of the C/C composite than $TaHfC_2$.

During the ablation of the C/C composite, many holes are formed because of the escaping of numerous gaseous products produced by the oxidation of carbon fibres and carbon matrix. These holes provide channels for the rapid oxygen diffusion, which in turn causes the severe chemical oxidation of the C/C composite within a short period of time. Unlike the ablation of the C/C composite, the following reactions occur during the ablation of the C/C-Ta_4HfC_5 and C/C-$TaHfC_2$ composites [25].

$$Ta_4HfC_5(s) + O_2(g) \rightarrow Ta_2O_5(l) + HfO_2(s) + CO(g) \quad (12)$$

$$TaHfC_2(s) + O_2(g) \rightarrow Ta_2O_5(l) + HfO_2(s) + CO(g) \quad (13)$$

$$Ta_2O_5(l) + HfO_2(s) \rightarrow Hf_6Ta_2O_{17}(s) \quad (14)$$

At the beginning of ablation, the Ta_4HfC_5 or $TaHfC_2$ solid solution at the surface of the composites is oxidised to produce Ta_2O_5 and HfO_2 (Eqs. (12) and (13)). Because ablation temperature is much higher than the melting point of Ta_2O_5 (~1800 °C), the formed Ta_2O_5 is melted into a melt with good fluidity. This melt can seal the holes formed by the oxidation of carbon fibres and carbon matrix and heal the cracks resulted from the mismatched thermal expansion between Ta_4HfC_5/$TaHfC_2$ and C/C substrates. Moreover, the melted Ta_2O_5 can react with HfO_2 to form $Hf_6Ta_2O_{17}$ (Eq. (14)) with high thermal stability and melting point (~2450 °C). The formed $Hf_6Ta_2O_{17}$ has a pinning effect on the molten Ta_2O_5 [26], which is favourable for improving the scouring

resistance of C/C-Ta_4HfC_5 and C/C-$TaHfC_2$ composites. In this study, the C/C-Ta_4HfC_5 composites show better anti-ablation performance as compared to the C/C-$TaHfC_2$ composites. This finding may be related to the difference in the composition and structure of the oxidation product of $TaHfC_2$ and Ta_4HfC_5 solid solutions, and the anti-ablation mechanism of the C/C-Ta_4HfC_5 and C/C-$TaHfC_2$ composites is still under investigation.

4. Conclusions and outlook

In this study, both the Ta_4HfC_5 and $TaHfC_2$ precursors were synthesised through a facile one-pot reaction. These two precursors were further utilised to prepare the C/C-Ta_4HfC_5 and C/C-$TaHfC_2$ composites through PIP. The conversion of Ta_4HfC_5 and $TaHfC_2$ precursors into ultra-fine ceramics and the ablation resistance of the C/C-Ta_4HfC_5 and C/C-$TaHfC_2$ composites were investigated. The main conclusions are as follows:

(1) Hf- and Ta-chelate structures, Ta–O–Ta and Hf–O–Hf bridges, as well as Ta–O–C and Hf–O–C chains are detected in the Ta_4HfC_5 precursor. This finding indicates that chelation and polycondensation occur in the one-pot reaction using $TaCl_5$, $HfCl_4$, and phenolic resins as raw materials.

(2) During the pyrolysis of the Ta_4HfC_5 precursor, amorphous carbon, Ta_2O_5, and $Hf_6Ta_2O_{17}$ are initially formed at temperatures below 1000 °C. Subsequently, carbothermal reduction between Ta_2O_5 and carbon begins at approximately 1000 °C. At 1200–1400 °C, the carbothermal reduction of Ta_2O_5 and $Hf_6Ta_2O_{17}$ and solid

solution reaction between HfC and TaC occur simultaneously. Finally, HfC and TaC undergo a sufficient solid solution reaction at 1800 °C to produce the Ta_4HfC_5 solid solution with a particle size of 200–300 nm.

(3) Ta_4HfC_5 particles are encapsulated in an amorphous shell with a thickness of about 3 to 4 nm. Ta, Hf, and C are homogeneously distributed in the Ta_4HfC_5 solid solution without any phase separation. The measured interplanar distance of Ta_4HfC_5 grains agrees well with the corresponding calculated value, which confirms its crystallised structure.

(4) The pyrolysis products of the $TaHfC_2$ precursor acquired at 1400–1600 °C are composed of TaC, HfC and $TaHfC_2$. High-temperature pyrolysis promotes the solid solution reaction between TaC and HfC. The $TaHfC_2$ solid solution with a particle size of 100–150 nm is formed at 1800 °C. In addition to the $TaHfC_2$ phase, residual carbon is also found in the pyrolysis product of the $TaHfC_2$ precursor at 1800 °C, and the ratio of bound carbon to residual carbon is approximately 0.63.

(5) $TaHfC_2$ particles are surrounded by an amorphous carbon layer with a thickness of 3 to 4 nm. The lattice fringe spacing of $TaHfC_2$ grains is in accordant with its theoretical calculated value.

(6) The introduction of $TaHfC_2$ and Ta_4HfC_5 solid solutions into the C/C composite substantially improves its anti-ablation performance. The linear ablation rates of the C/C-Ta_4HfC_5 and C/C-$TaHfC_2$ composites are 11.04 and 16.97 μm/s, respectively, which are much lower than that of the C/C composite. Ta_4HfC_5 presents more advantages in improving the anti-ablation of the C/C composite than $TaHfC_2$.

(7) The good anti-ablation performance of C/C- Ta_4HfC_5 and C/C-$TaHfC_2$ composites can be ascribed to the generation of the Ta_2O_5 and $Hf_6Ta_2O_{17}$. The formed Ta_2O_5 acts as an oxygen diffusion barrier, and $Hf_6Ta_2O_{17}$ improves the scouring resistance of the composites.

The C/C-Ta_4HfC_5 and C/C-$TaHfC_2$ composites have good anti-ablation performance at ultra-high temperatures. However, they can be expected to exhibit poor anti-ablation performance in low/medium-temperature environments. This is mainly because the oxidation products of Ta_4HfC_5 and $TaHfC_2$ are solids with high melting points, which cannot form a protective oxide film to inhibit oxygen diffusion. In order to broaden the anti-ablation temperature range of the C/C-Ta_4HfC_5 and C/C-$TaHfC_2$ composites, SiC-Ta_4HfC_5 and SiC-$TaHfC_2$ hybrid precursors will be synthesised and used to prepare SiC-Ta_4HfC_5 and SiC-$TaHfC_2$ modified C/C composites, considering that SiC has desirable oxidation resistance at medium temperatures. The anti-ablation performance and ablation mechanisms of the SiC-Ta_4HfC_5- and SiC-$TaHfC_2$-modified C/C composites will be further investigated in the future.

Acknowledgments

The authors acknowledge the financial support from the Natural Science Foundation of China (No. U1960106, 52072275, U1864207 and 52002296).

Reference

[1] Y. Lu, Y. Sun, T. Zhang, F. Chen, Ye, L.; Zhao, T., Polymer-derived Ta_4HfC_5

nanoscale ultrahigh-temperature ceramics: Synthesis, microstructure and properties, J. Eur. Ceram. Soc. 39 (2019) 205–211.

[2] J. Jiang, W. Song, L. Wei, Preparation and characterization of ultrahigh-temperature ternary ceramics Ta_4HfC_5, J. Am. Ceram. Soc. 99 (2016) 3198–3201.

[3] J. Zhang, S. Wang, W. Li, Nano-scale 1TaC-3HfC solid solution powder synthesized using a solvothermal method and its densification, Ceram. Int. 45 (2019) 1455–1459.

[4] A.A. Lavrentyev, B.V. Gabrelian, V.B. Vorzhev, I.Y. Nikiforov, O.Y. Khyzhun, J.J. Rehr, Electronic structure of cubic $Hf_xTa_{1-x}C_y$ carbides from X-ray spectroscopy studies and cluster self-consistent calculations, J. Alloys. Compd. 462 (2008) 4–10.

[5] O. Gaballa, B.A. Cook, A.M. Russell, Reduced-temperature processing and consolidation of ultra-refractory Ta_4HfC_5, Int. J. Refract. Met. H. 41 (2013) 293–299.

[6] O. Cedillos-Barraza, S. Grasso, N. Al Nasiri, D.D. Jayaseelan, M.J. Reece, W.E. Lee, Sintering behaviour, solid solution formation and characterisation of TaC, HfC and TaC-HfC fabricated by spark plasma sintering, J. Eur. Ceram. Soc. 36 (2016) 1539–1548.

[7] S.A. Ghaffari, M.A. Faghihi-Sani, F. Golestani-Fard, S. Ebrahimi, Pressureless sintering of $Ta_{0.8}Hf_{0.2}C$ UHTC in the presence of $MoSi_2$, Ceram. Int. 39 (2013) 1985–1989.

[8] L. Feng, J.M. Kim, S.H. Lee, and S.J. Park, Synthesis of a fine $(Ta_{0.8},Hf_{0.2})C$ powder from carbide or oxide powder mixtures, J. Am. Ceram. Soc. 99 (2016) 1129–1132.

[9] E.P. Simonenko, N.P. Simonenko, M.I. Petrichko, V.G. Sevastyanov, and N.T. Kuznetsov, Sol-gel synthesis of highly dispersed tantalum hafnium carbide Ta_4HfC_5, Russ. J. Inorg. Chem. 64 (2019) 1317–1324.

[10] E.P. Simonenko, N.A. Ignatov, N.P. Simonenko, Y.S. Ezhov, V.G. Sevastyanov, N.T. Kuznetsov, Synthesis of highly dispersed super-refractory tantalum-zirconium carbide Ta_4ZrC_5 and tantalum-hafnium carbide Ta_4HfC_5 via sol-gel technology, Russ. J. Inorg. Chem.56 (2011) 1681–1687.

[11] K. Inzenhofer, T. Schmalz, B. Wrackmeyer, and G. Motz, The preparation of HfC/C ceramics via molecular design, Dalton Trans. 40 (2011) 4741–4745.

[12] T. Cai, W.F. Qiu, D. Liu, W.J. Han, L. Ye, A.J. Zhao, and T. Zhao, Synthesis, characterization, and microstructure of hafnium boride-based composite ceramics via preceramic method, J. Am. Ceram. Soc. 96 (2013) 1999–2004.

[13] Y.N. Sun, C.M. Yang, Y. Lu, F.H. Chen, Transformation of metallic polymer precursor into nanosized $HfTaC_2$ ceramics. Ceram. Int. (46) 2020 6022–6028.

[14] O. Cedillos-Barraza, S. Grasso, N.A. Nasiri, D.D. Jayaseelan, M.J. Reece, W.E. Lee, Sintering behaviour, solid solution formation and characterisation of TaC, HfC and TaC–HfC fabricated by spark plasma sintering, J. Eur. Ceram. Soc. 36 (2016) 1539–1548.

[15] Z. Zhang, C.Q. Fang, L. Chen, X. Yang, A.H. Shi, Q.Z. Huang, H.P. Hu, Fabrication, microstructure and ablation resistance of C/C–SiC composites, by using a novel precursor of SiC. Ceram. Int. 47 (2021) 7224–7232.

[16] J.F. Moulder, J. Chastain, R.C. King, Handbook of X-ray photoelectron

spectroscopy: a reference book of standard spectra for identification and interpretation of XPS data. Chem. Phys. Lett., 220(1992) 7–10.

[17] Brian H. Toby. EXPGUI, a graphical user interface for GSAS. J. Appl. Crystallogr., 34(2001) 210–213.

[18] T. Cai, D. Liu, W. F. Qiu, W.J. Han, T. Zhao, Polymer precursor derived HfC-SiC ultrahigh-temperature ceramic nanocomposites, J. Am. Ceram. Soc. 101 (2017) 20–24.

[19] J.M. Jiang, S. Wang, W. Li, Z.H. Chen, Low-temperature synthesis of tantalum carbide by facile one-pot reaction, Ceram. Int. 42 (2016) 7118–7124.

[20] C. Liu, W.M. Wang, Q.L. He, A.Y. Wang, J. Wu, H. Wang, J.Y. Zhang, Z.Y. Fu, Synthesis of ultra-fine tantalum carbide powders by a combinational method of sol–gel and spark plasma sintering, Ceram. Int. 44 (2018) 19106–19112.

[21] Y.L. Xie, H. Thomas, J. Sanders, and F. Robert, Solution-based synthesis of submicrometer ZrB_2 and ZrB_2–TaB_2, J. Am. Ceram. Soc. 91(2008)1469–1474.

[22] S.A. Ghaffari, M.A. Faghihi-Sani, F. Golestani-Fard, M. Nojabayy, Diffusion and solid solution formation between the binary carbides of TaC, HfC and ZrC, Int. J. Refract. Met. H. 41 (2013) 180–184.

[23] O.Y. Khyzhun, E.A. Zhurakovsky, A.K. Sinelnichenko, V. A. Kolyagin, Electronic structure of tantalum subcarbides studied by XPS, XES, and XAS methods, J. Electron Spectrosc. Relat. Phenom. 82 (1996) 179–192.

[24] J. Cheng, J. Wang, X. Wang, W. Hao, Preparation and high-temperature performance of HfC-based nanocomposites derived from precursor with Hf-(O,N)

bonds, Ceram. Int. 43 (2017) 7159–7165.

[25] C. Zhang, B. Boesl, A. Agarwal. Oxidation resistance of tantalum carbide-hafnium carbide solid solutions under the extreme conditions of a plasma jet, Ceram. Int. 43 (2017) 14798–14806.

[26] Y.L. Zhang, D.Y. Shao, G.H. Feng, Y.Q. Fu, J. Li, Ablation-resistant Ta0.78Hf0.22C solid solution ceramic modified C/C composites for oxidizing environments over 2200 °C, J. Eur. Ceram. Soc. 41 (2021) 6181–6188.

Figures and tables

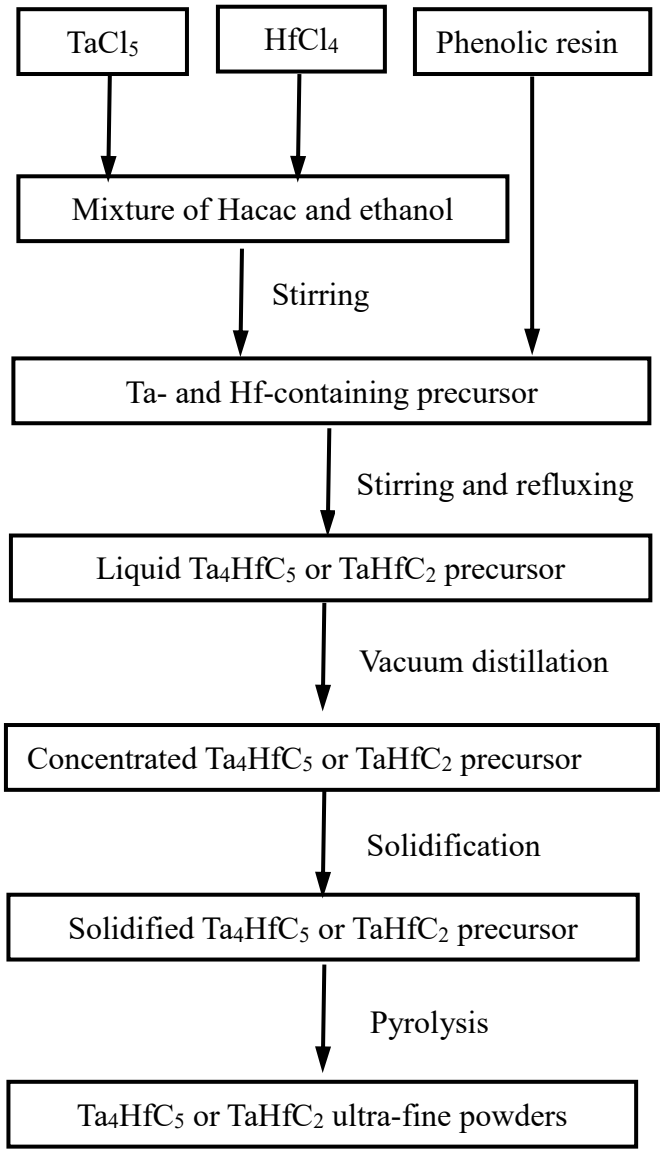

Fig. 1 Flow chart for the synthesis of Ta_4HfC_5 and $TaHfC_2$ ultra-fine powders from their organometallic precursors

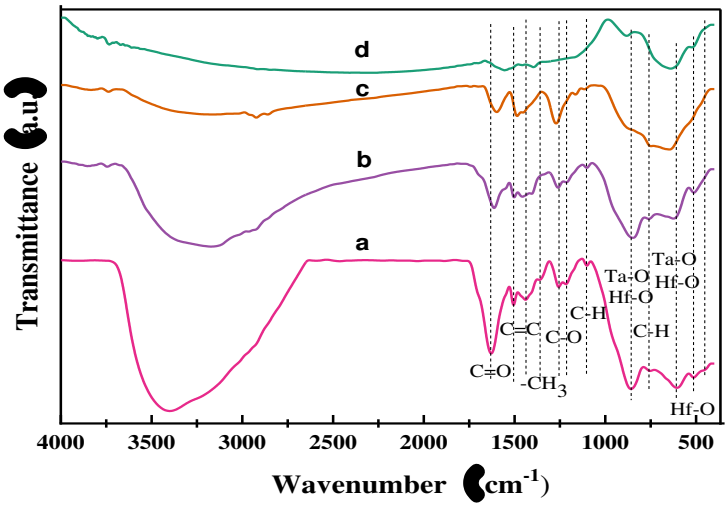

Fig. 2 FTIR spectra of (a) Ta_4HfC_5 precursor, and its products pyrolysed at (b) 200 °C, (c) 400 °C, and (d) 600 °C

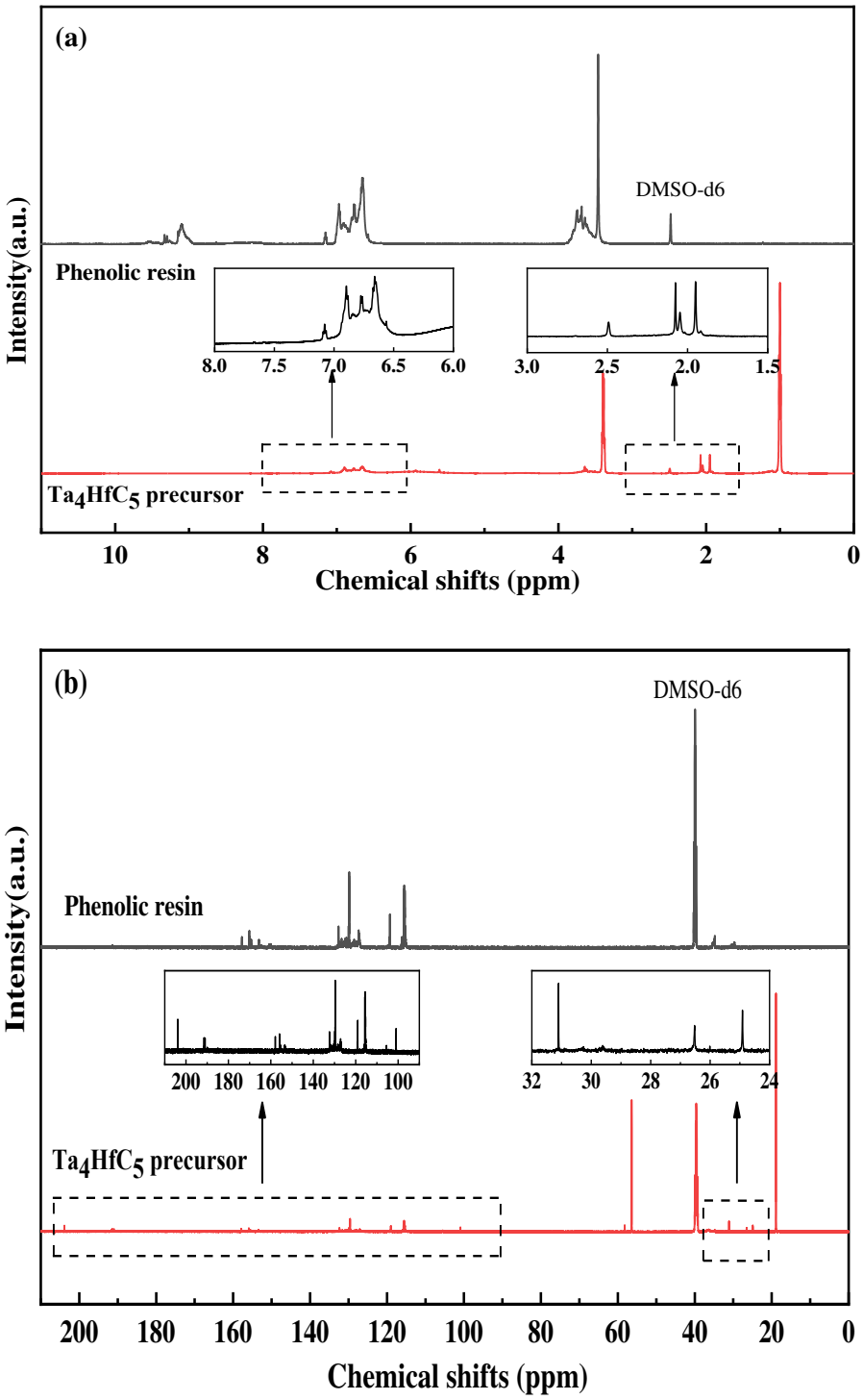

Fig. 3 (a) ^{1}H NMR and (b) ^{13}C NMR spectra of the phenolic resin and Ta_4HfC_5 precursor

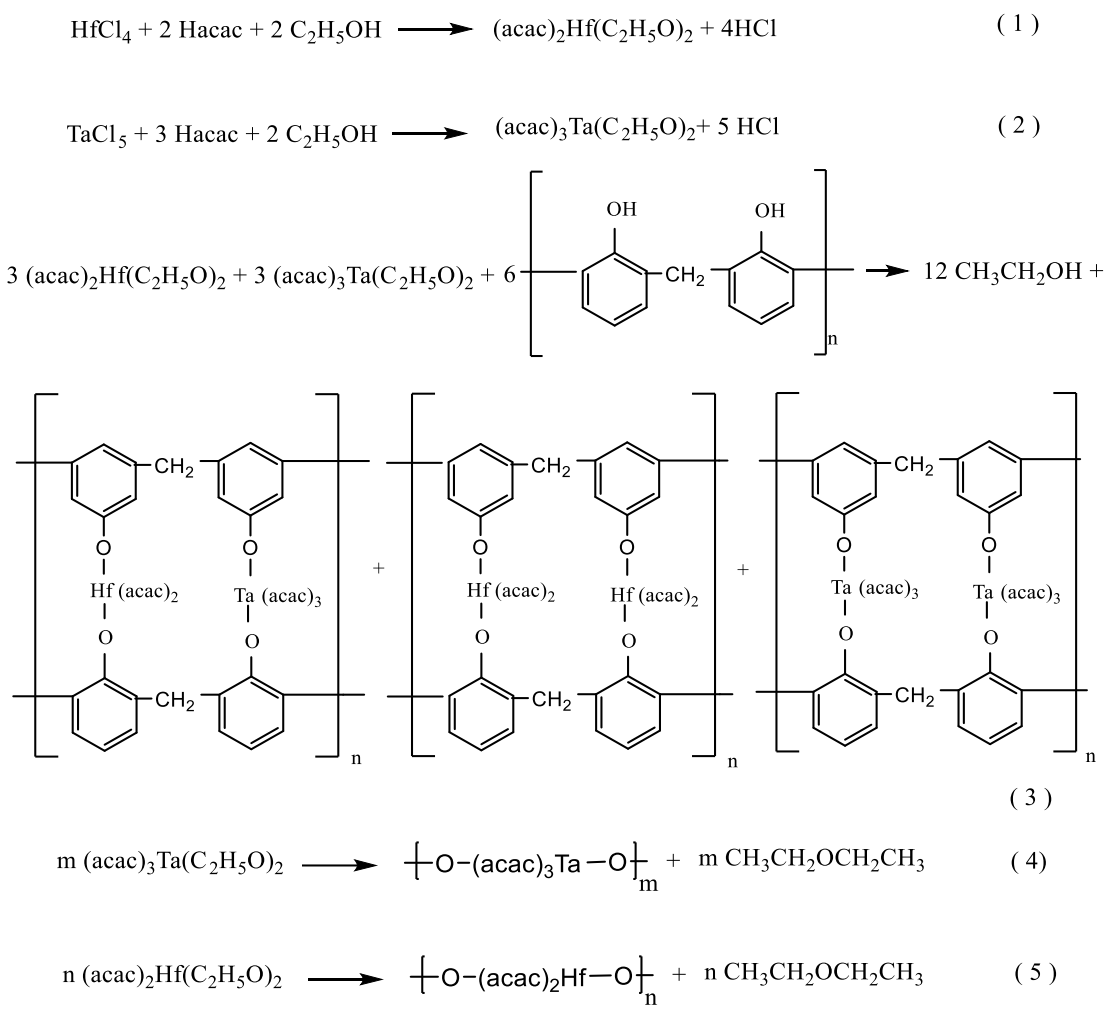

Fig. 4 Possible synthesis route to the Ta_4HfC_5 and $TaHfC_2$ precursors

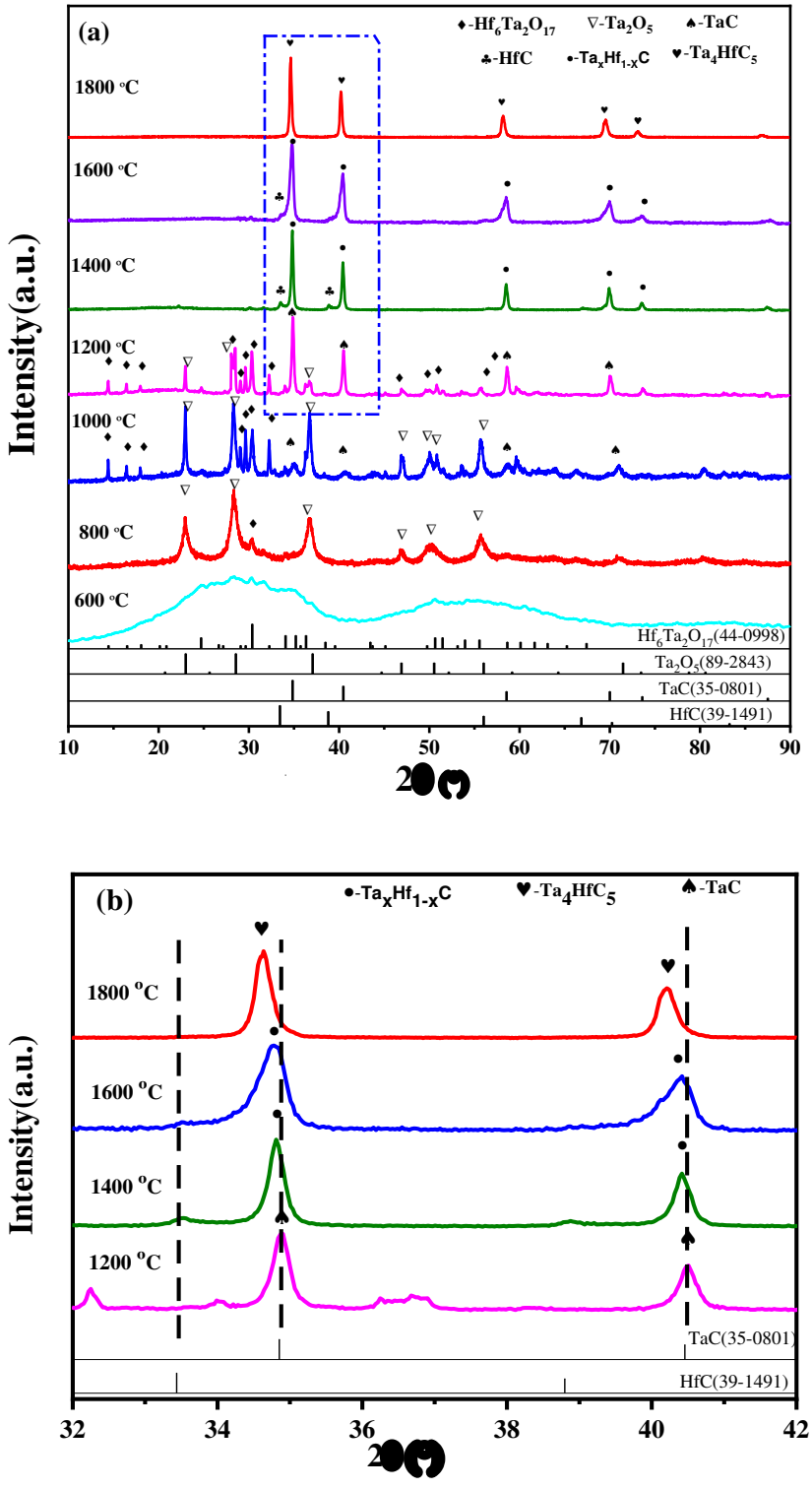

Fig. 5 (a) XRD spectra for the products pyrolysed from Ta_4HfC_5 precursor at 600–1800 °C; (b) magnified diffraction spectra between 32° and 42° 2θ angles in (a) displaying shift of diffraction peaks during formation of Ta_4HfC_5 solid solutions

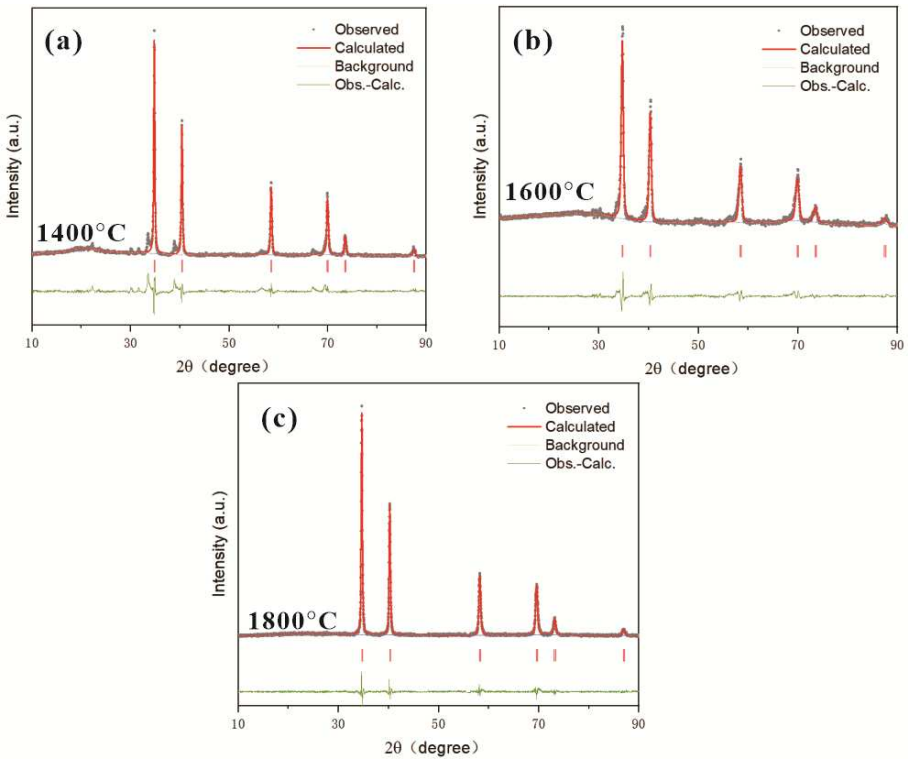

Fig. 6 Rietveld refinement plots of the XRD patterns for the $Ta_xHf_{1-x}C$ solid solution obtained at (a) 1400 °C, (b) 1600 °C and (c) 1800 °C

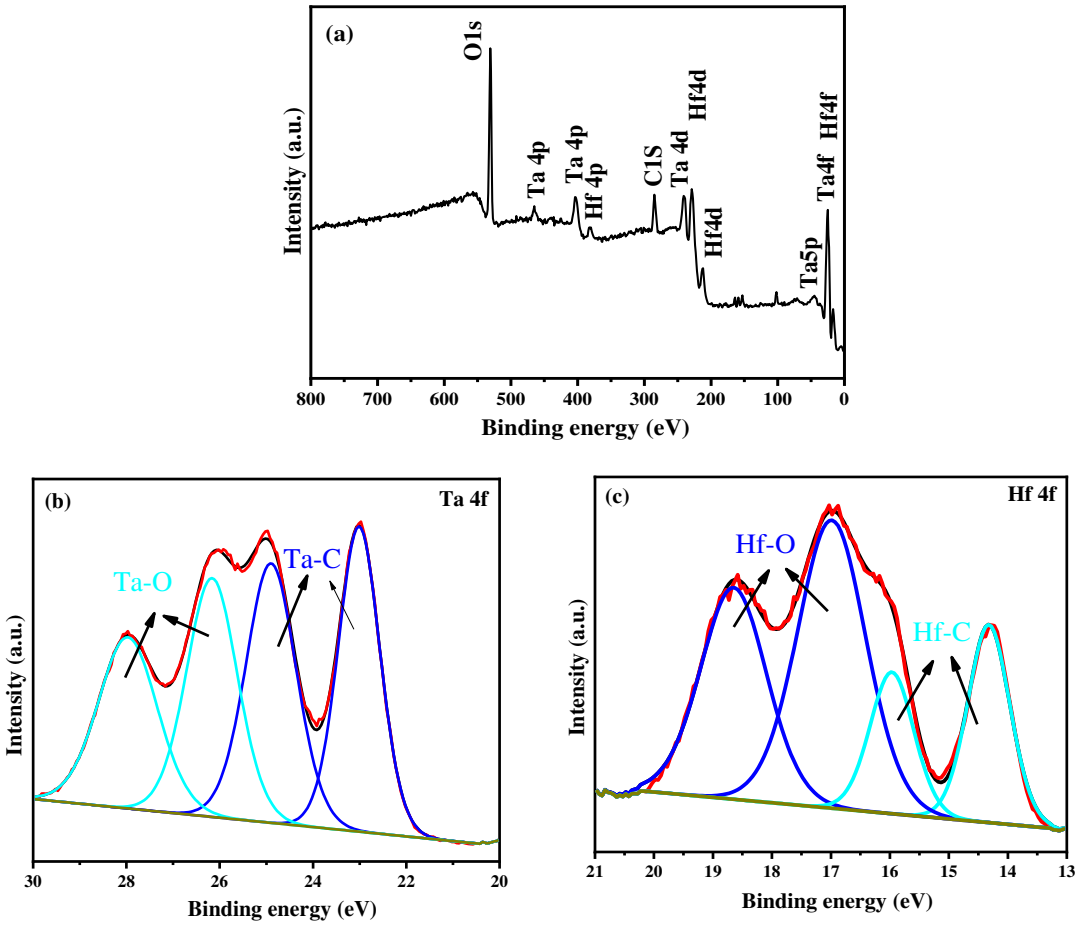

Fig. 7 (a) XPS survey spectrum and fitted spectra of (b) Ta 4f and (c) Hf 4f for the product obtained from the pyrolysis of Ta_4HfC_5 precursors at 1300 °C

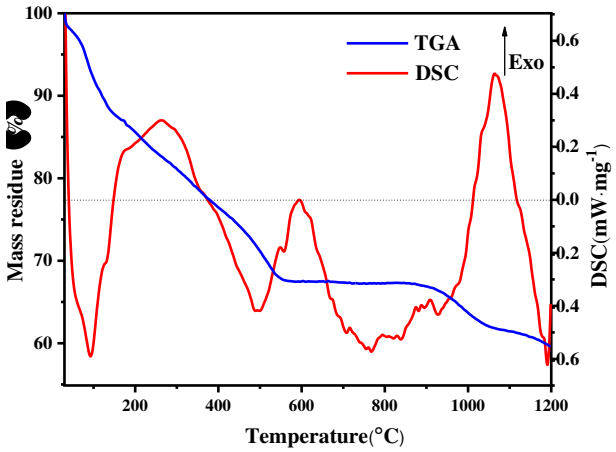

Fig. 8 TGA-DSC curves of the Ta_4HfC_5 precursor

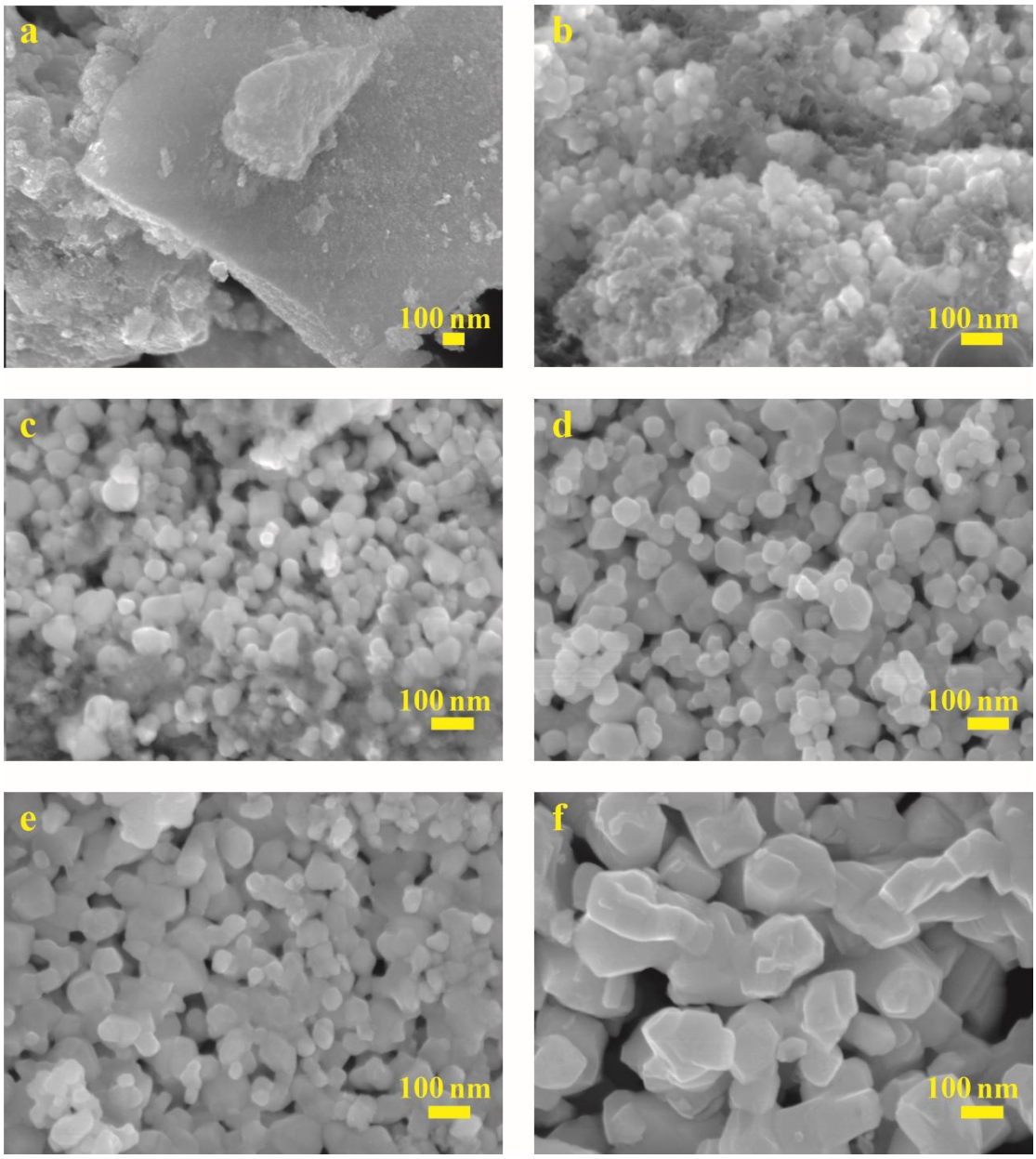

Fig. 9 SEM images of the various pyrolysis products from the Ta_4HfC_5 precursor at (a) 600 °C , (b) 1000 °C , (c) 1200 °C, (d) 1400 °C, (e) 1600 °C, and (f) 1800 °C

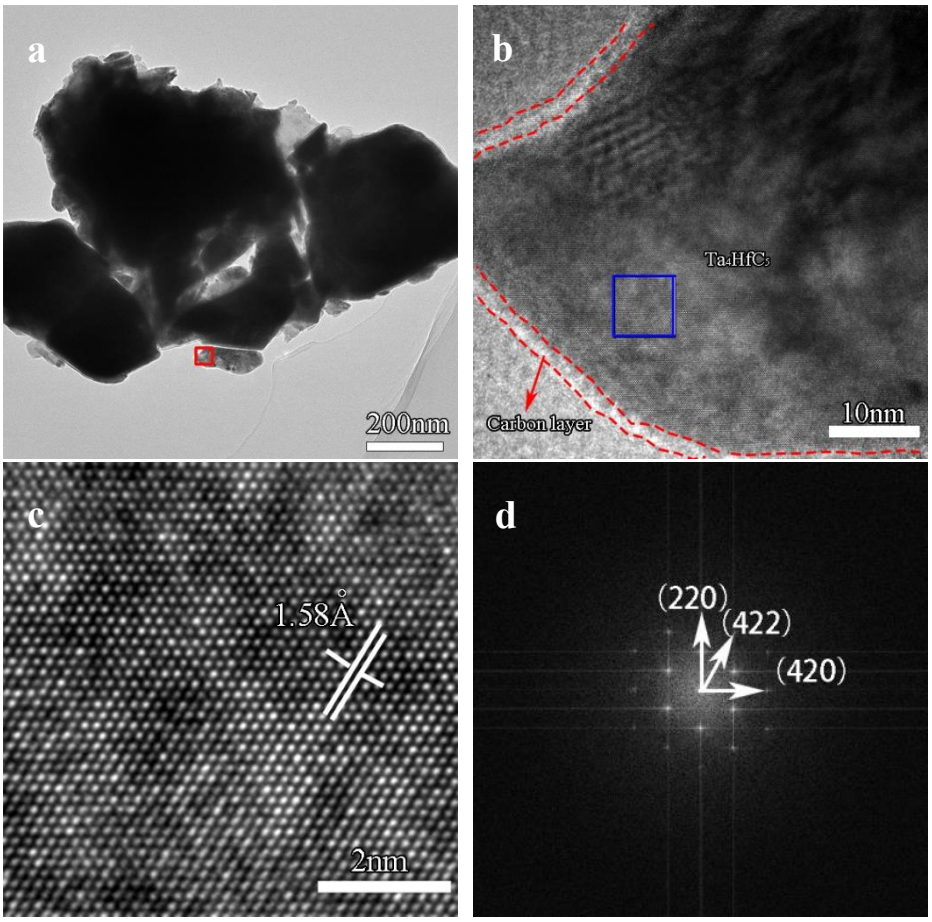

Fig. 10 (a) TEM and (b) HRTEM images of Ta_4HfC_5 powders prepared through precursor pyrolysis at 1800 °C. (c) Enlarged view of the rectangle in (b) showing the lattice spacing. (d) FFT transformation of (b) obtained using digital micrograph software

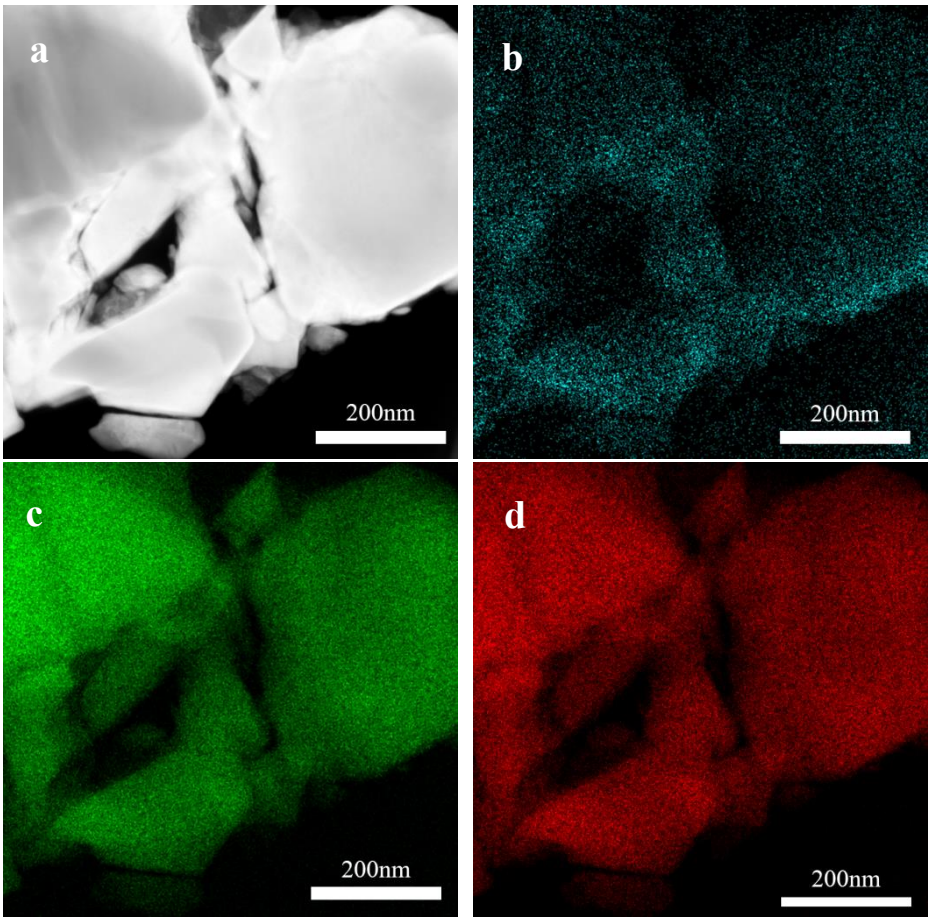

Fig. 11 (a) TEM image of the Ta_4HfC_5 powder prepared through the pyrolysis of precursors at 1800 °C and relevant distributions of (b) C, (c) Ta, and (d) Hf elements

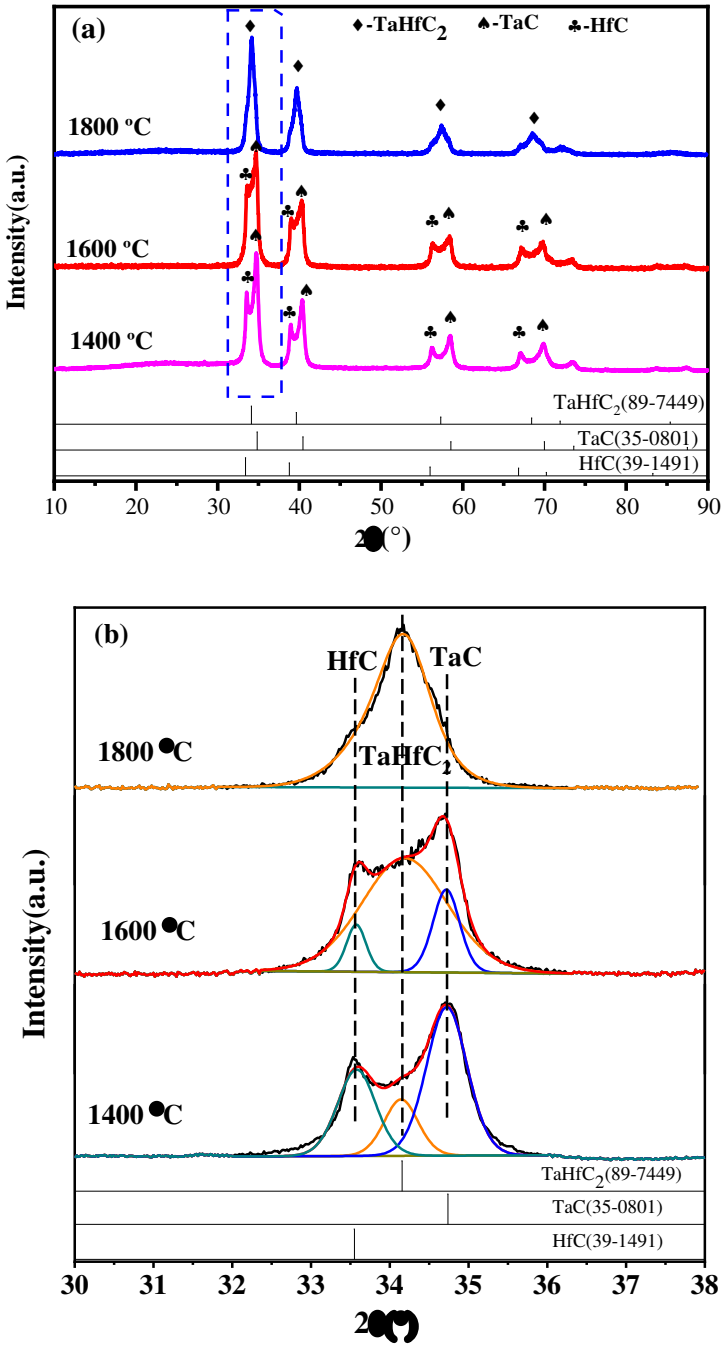

Fig. 12 (a) XRD spectra for the products of $TaHfC_2$ precursor pyrolysis implemented from 1400 to 1800 °C, and (b) fitting of the diffraction patterns between 30° and 38° 2θ angles in (a) showing the formation of $TaHfC_2$ solid solutions

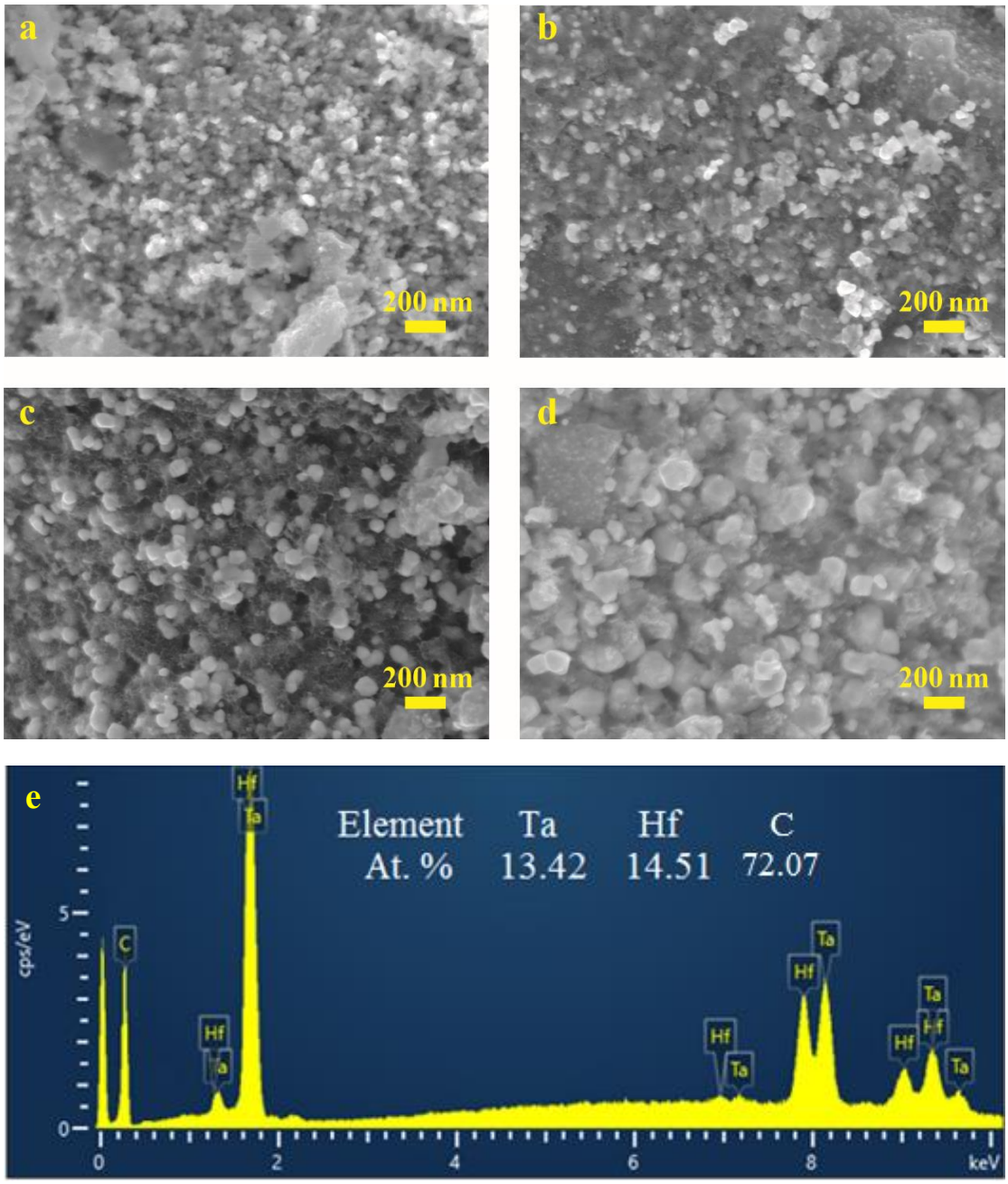

Fig. 13 SEM micrographs for the products of $TaHfC_2$ precursor pyrolysed at (a) 1200, (b) 1400, (c) 1600, and (d) 1800 °C. (e) EDS pattern for the pyrolysis product obtained at 1800 °C

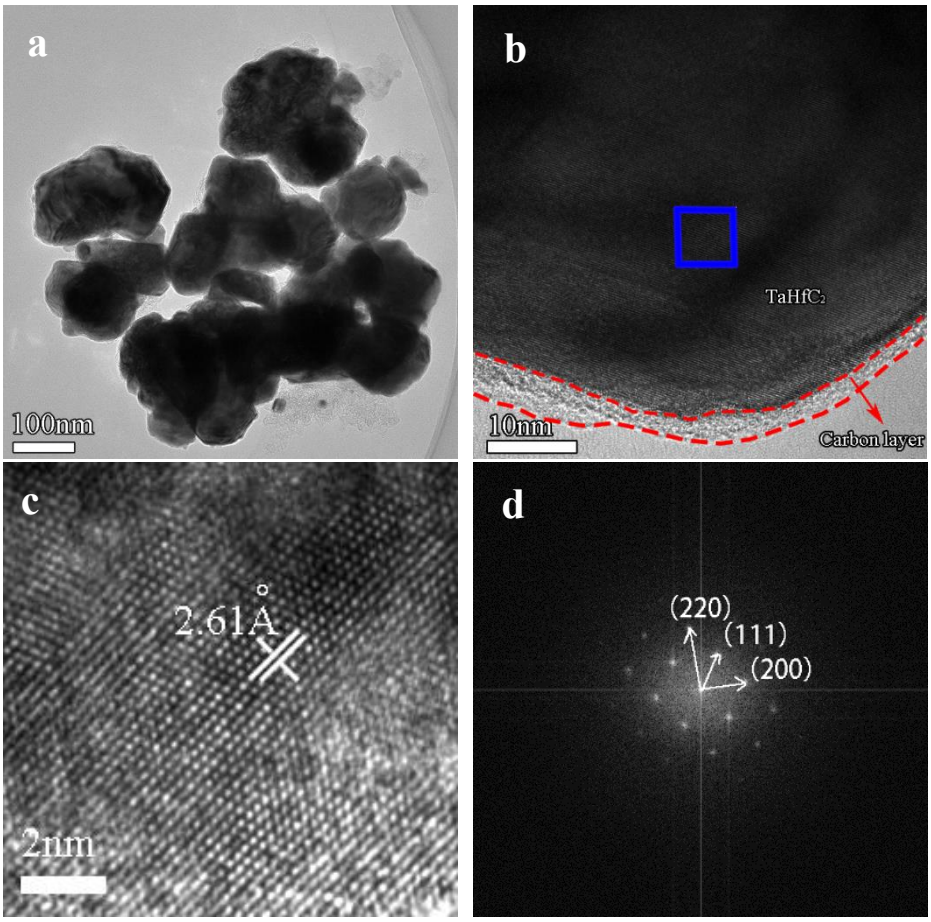

Fig. 14 (a) TEM and (b) HRTEM micrographs of the $TaHfC_2$ powders prepared through precursor pyrolysis at 1800 °C, (c) enlarged view of the rectangle in (b), and (d) FFT transformation of (c) obtained using digital micrograph software

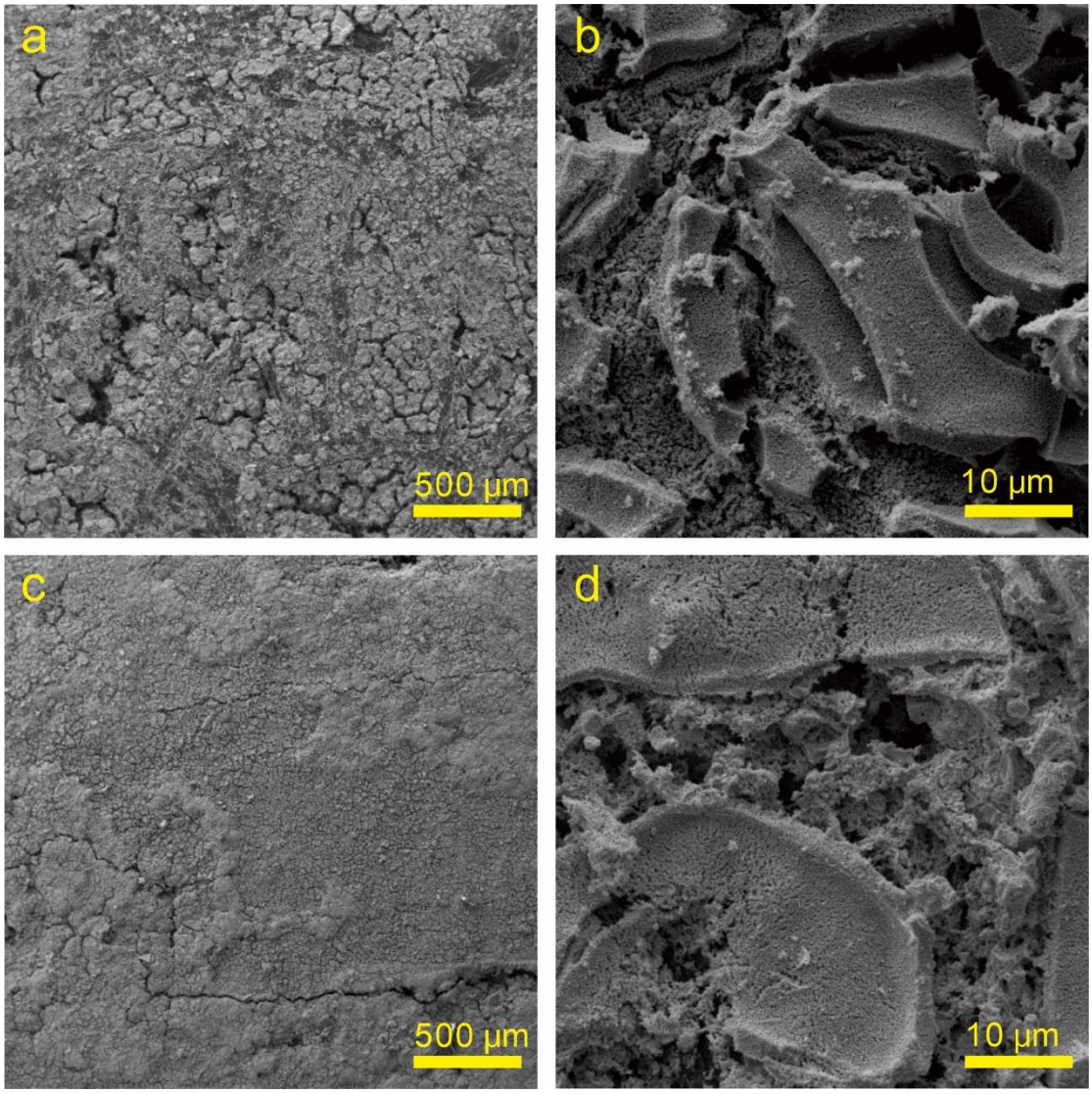

Fig. 15 Surface SEM images of (a, b) C/C-Ta_4HfC_5 and (c, d) C/C-$TaHfC_2$ composites

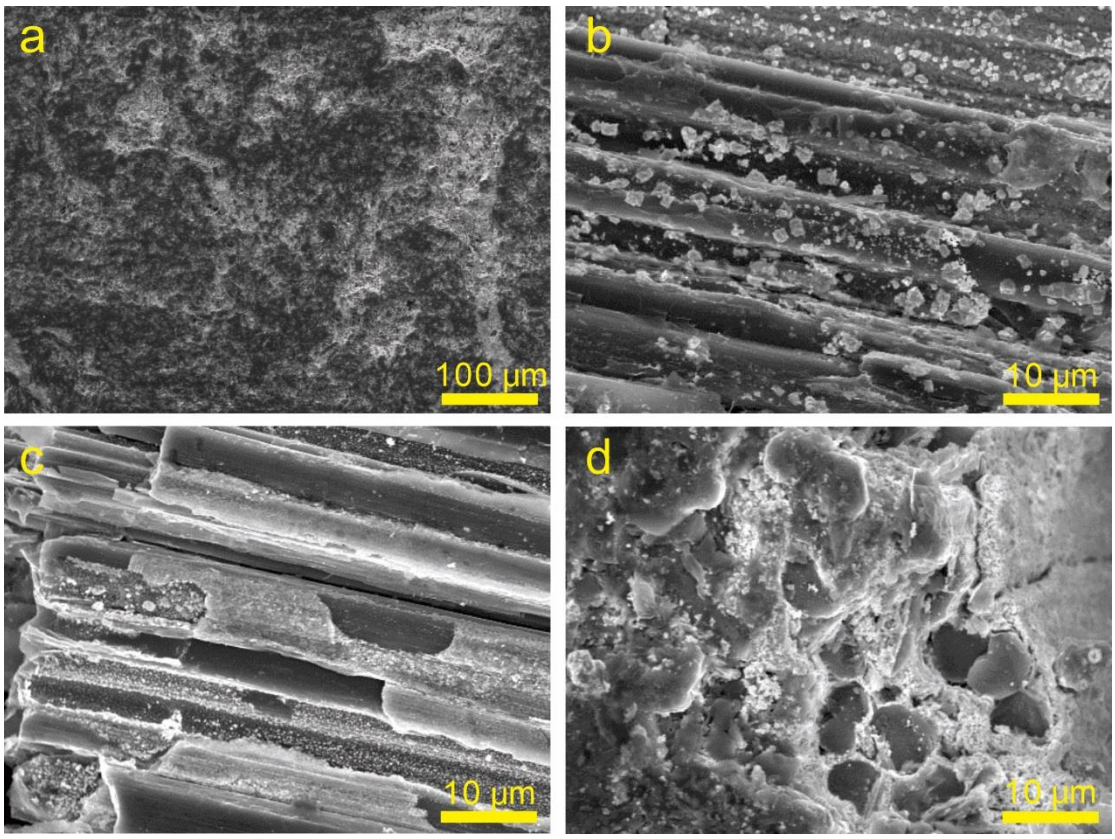

Fig. 16 Cross-sectional SEM images of the C/C-Ta_4HfC_5 composite

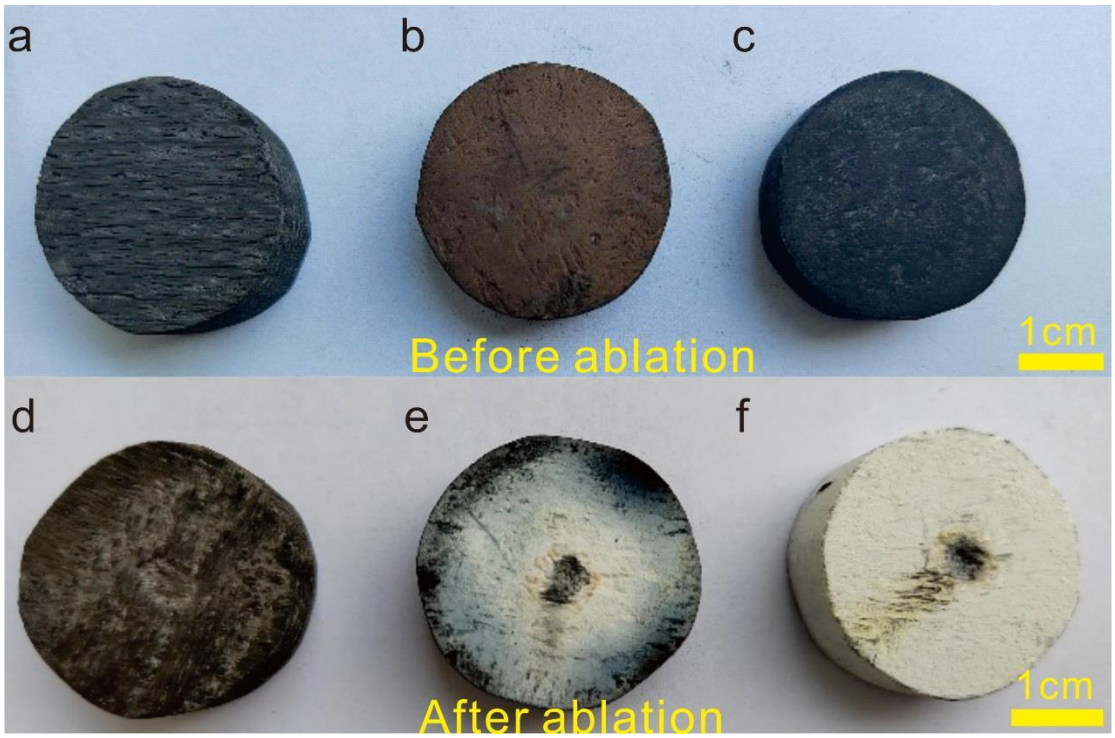

Fig. 17 Photographs of C/C, C/C-Ta_4HfC_5 and C/C-$TaHfC_2$ composites before and after ablation: (a, d) C/C composites; (b, e) C/C-Ta_4HfC_5 composites; (c, f) C/C-$TaHfC_2$ composites

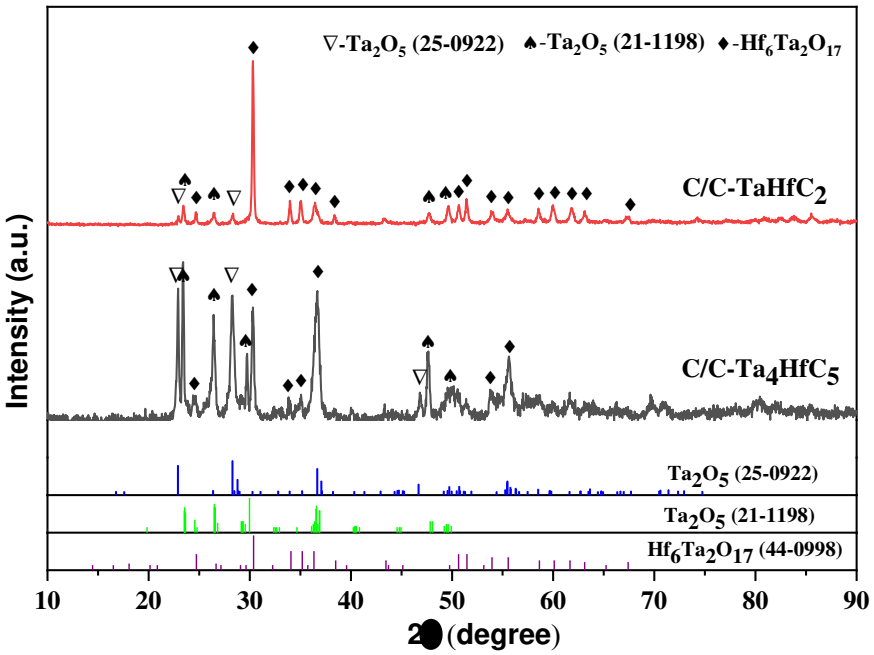

Fig. 18 XRD patterns of the C/C-Ta_4HfC_5 and C/C-$TaHfC_2$ composites after ablation

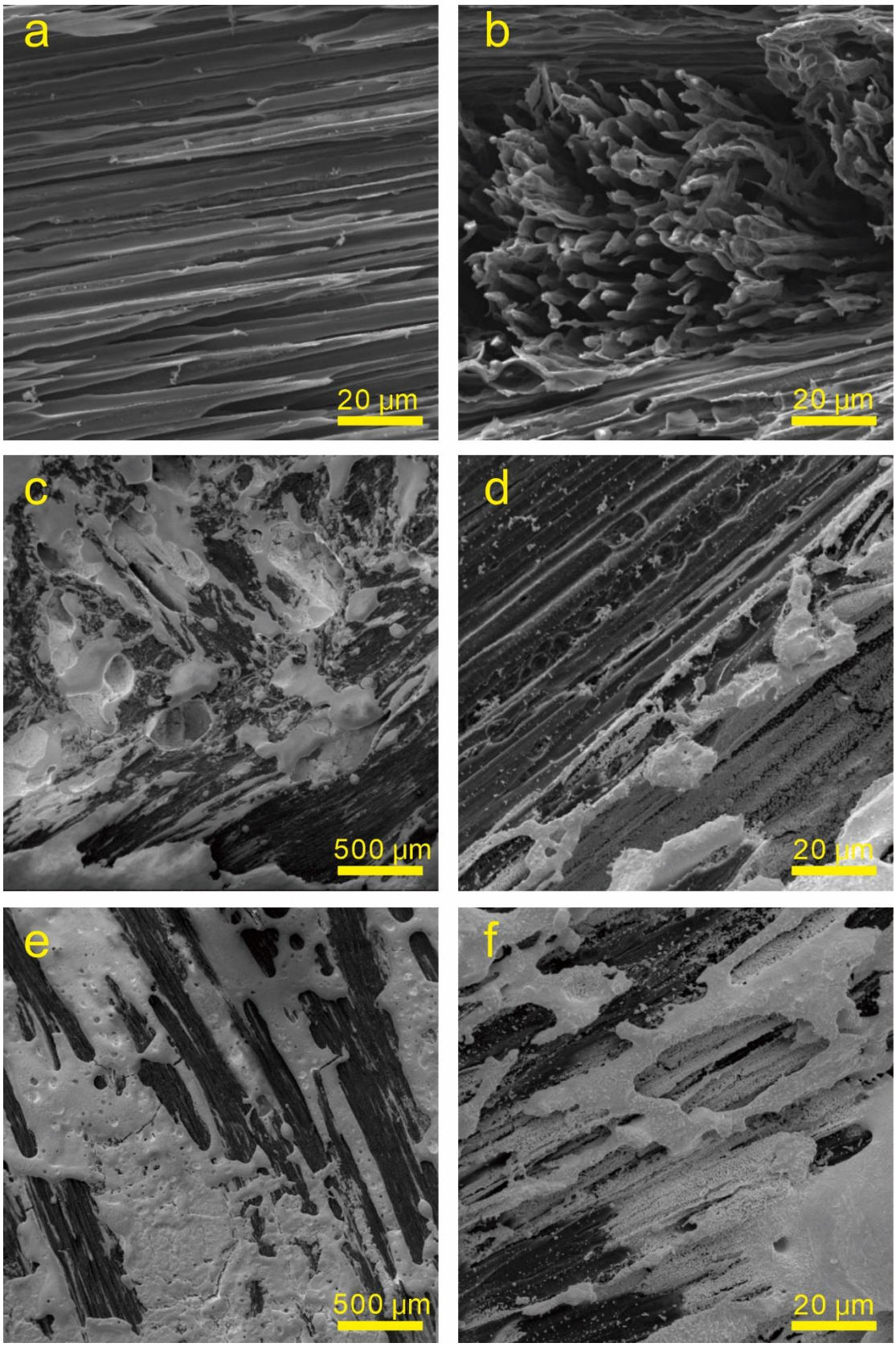

Fig. 19 SEM images of ablation centres of (a, b) C/C, (c, d) C/C-Ta_4HfC_5, and (e-f) C/C-$TaHfC_2$ composites

Table 1 Refinement results of the $Ta_xHf_{1-x}C$ solid solution

Samples	Lattice constant (Å)	Lattice volume ($Å^3$)	Solid solubility of Hf (1-x)
S400	4.455532	88.450	0.11
S1600	4.458656	88.636	0.16
S1800	4.484165	90.166	0.20

Note: S400, S1600 and S1800 are the $Ta_xHf_{1-x}C$ solid solution obtained at 1400 °C, 1600 °C and 1800 °C, respectively.

Table 2 Ablation properties of the C/C, C/C-Ta_4HfC_5 and C/C-$TaHfC_2$ composites

Samples	Density (g/cm^3)	Linear ablation rate (μm/s)	Mass ablation rate (mg/s)
C/C	1.20	23.45	5.66
C/C-Ta_4HfC_5	2.07	11.04	-1.22
C/C- $TaHfC_2$	2.00	16.97	-1.46